University of Naples Federico II

Department of Chemical, Materials and Industrial
Production Engineering

XXXV° Ph.D. Programme in
Industrial Products and Processes Engineering

Ph.D. Thesis

Numerical simulation and experimental study of the powder spreading process in additive manufacturing

Ph.D Course Coordinator
Ch.mo Prof. Andrea D’Anna

Ph.D. Candidate
Valerio Lampitella

Ph.D. Supervisors
Prof.AntonelloAstarita
Prof. Gaetano D’Avino

Contents

Section 1: State of the art 1
Section 2: Experimental analysis 8
2.1 Materials and methodology 8
2.1.1 The experimental device 8
2.1.2 The feedstock materials 9
2.1.3 Powder bed characterization 11
2 .2 Results 15
2.2.1 Poor grade feedstock material 15
2.2.2 Good grade feedstock material 19
Section 3: Numerical model 24
3.1 The Discrete Element Method 24
3.2 Calibration procedure 30
3.3 Simulation setup 35
3.4 Results 37
3.4 Parallelization 44
3.5 Multilayer 52
3.5 Influence of a solid part 67
Section 4: Application 73
4.1 Motivation 73
4.2 Materials and methods 75
4.2.1 Feedstock material 75
4.2.2 Optimization of the spreading process 77
4.2.3 Printed samples characterization 81
4.3 Results 84
4.3.1 Surface roughness 84
4.3.2 Density 86
4.3.3 Microstructure 91

4.3.4 Microhardness 93
4.4 Discussion 94
4.4.1 The role of the powder bed and laser power 94
4.4.2 Comparison with the literature 95
Section 5: Future developments 98
Section 6: Conclusions 101
Bibliography 105

List of figures

Figure 1 - Experimental device used in the spreading experiments. 8

Figure 2 - SEM image of the “poor grade” feedstock material. 10

Figure 3 - (Left) SEM image of the "good grade" feedstock material. (Right) Particle Size Distribution of the "good grade" material. 11

Figure 4 - Position of the sampling zones in the deposition plate. 12

Figure 5 - Relative packing density at “rear” and “front” locations for the “poor grade" feedstock material for a layer thickness of 100 μm. . 17

Figure 6 - Relative packing density at “rear” and “front” locations for the “poor grade" feedstock material for a layer thickness of 50 μm. 17

Figure 7 - Relative packing density at “rear” and “front” locations for the “poor grade" feedstock material for a layer thickness of 30 μm. 18

Figure 8 - Percentage of the in-focus zone for the different zones of the powder bed (blue cross) and its average value (red dot). 19

Figure 9 - Relative packing density at “rear” and “front” locations for the “good grade" feedstock material for a layer thickness of 100 μm. 20

Figure 10 - Relative packing density at “rear” and “front” locations for the “good grade" feedstock material for a layer thickness of 50 μm. 20

Figure 11 - Relative packing density at “rear” and “front” locations for the “good grade" feedstock material for a layer thickness of 30 μm. 21

Figure 12 - Working principle of the Discrete Element Method. 26

Figure 13 - Procedure for the calculation of the angle of repose. 32

Figure 14 - Directions along which the angle of repose is calculated. 32

Figure 15 - Experimental setup for the calculation of the angle of repose... 33

Figure 16 - Variation of the angle of repose with coefficient of friction and Cohesion Energy Density and optimal value (red cross). 34
Figure 17 - Variation of the slipping angle with coefficient of friction and Cohesion Energy Density and optimal value (red cross). 34
Figure 18 - Setup used for the simulations with relevant dimensions. 35
Figure 19 - State of the powder feedstock after the settling of the particles. 38
Figure 20 - Dynamic angle of repose in the accumulation stage for two different speeds of the blade: (**a**) 20mm/s, (**b**) 100mm/s. 39
Figure 21 - Snapshot of the base of the powder heap, where a front formed by the bigger particles can be observed. The picture is referred to a 20mm/s spreading speed. 40
Figure 22 - Typical state of the powder bed after the spreading process at (a) 100mm/s and (b) 20mm/s. (c) Relative density, (d) effective thickness, and (e) mean diameter of the layer of powder along the spreading direction. 42
Figure 23 - Phases during a timestep. 47
Figure 24 - Simulation time (total and phase wise) for 10k timesteps with 320k particles for different numbers of processors. 48
Figure 25 - Simulation time (phase wise) for 10k timesteps with 320k particles for different numbers of processors in double log scale. 49
Figure 26 - speedup relative to 4 processors for 10k timesteps with 320k particles. 51
Figure 27 – Relationship between input and output of layer n and layer n+1 54
Figure 28 - a) Effective Layer Thickness and b) solid volume fraction theory for layer 1 56

Figure 29 - a) Effective Layer Thickness, b) Real Effective Layer Thickness c) soldi volume fraction theory and d) solid volume fraction real for layer 2. 56
Figure 30 - a) Effective Layer Thickness, b) Real Effective Layer Thickness c) soldi volume fraction theory and d) solid volume fraction real for layer 3. 57
Figure 31 - a) Effective Layer Thickness, b) Real Effective Layer Thickness c) soldi volume fraction theory and d) solid volume fraction real for layer 4. 58
Figure 32 - a) Effective Layer Thickness, b) Real Effective Layer Thickness c) soldi volume fraction theory and d) solid volume fraction real for layer 5. 59
Figure 33 - Value of the real effective layer thickness as a function of layers for the combination of parameters number 1 in table 6.............. 62
Figure 34 - Value of the real effective layer thickness as a function of layers for the combination of parameters number 2 in table 6.............. 62
Figure 35 - Value of the real effective layer thickness as a function of layers for the combination of parameters number 3 in table 6.............. 63
Figure 36 - Value of the real effective layer thickness as a function of layers for the combination of parameters number 4 in table 6.............. 63
Figure 37 - Value of the real effective layer thickness as a function of layers for the combination of parameters number 5 in table 6.............. 64
Figure 38 - Value of the real effective layer thickness as a function of layers for the combination of parameters number 6 in table 6.............. 64
Figure 39 - Value of the real effective layer thickness as a function of layers for the combination of parameters number 7 in table 6.............. 65
Figure 40 - Value of the real effective layer thickness as a function of layers for the combination of parameters number 8 in table 6.............. 65

Figure 41 - Value of the real effective layer thickness as a function of layers for the combination of parameters number 9 in table 6.............. 66
Figure 42 - Value of the real effective layer thickness as a function of layers for the combination of parameters number 10 in table 6............ 66
Figure 43 - Procedure used to mesh the layer: a) generation of the point cloud, b) binning and finding the max point per bin, c) reconstruction of the mesh.. 68
Figure 44 - Solid volume fraction real with meshed substrate for layer number 2. 70
Figure 45 - Solid volume fraction real with meshed substrate for layer number 3. 70
Figure 46 - Solid volume fraction real with meshed substrate for layer number 4. 71
Figure 47 - Solid volume fraction real with meshed substrate for layer number 5. 71
Figure 48 - SEM images of the powders used as base materials: (a) AlSi10Mg; (b) Cu.. 75
Figure 49 - SEM image of the mixed powder used as feedstock material. The Cu particles 76
Figure 50 - Results of the simulations with a 30 μm layer thickness for different levels of spreading speeds: (a) 75 mm/s, (b) 50 mm/s, and (c) 25 mm/s.. 77
Figure 51 - Results of the simulations with a 50 μm layer thickness for different levels of spreading speed: (a) 75 mm/s, (b) 50 mm/s, and (c) 25 mm/s.. 78
Figure 52 - Surface coverage for different spreading velocities and layer thicknesses... 79

Figure 53 - Solid volume fraction for different spreading velocities and layer thicknesses. 80
Figure 54 - Steps of image analysis: (a) optical acquisition of the cross-section, (b) identification of the porosities, (c) image mask. 83
Figure 55 - Overview of the printed samples with the respective processing conditions... 84
Figure 56 - Rendering of the acquired top surface of sample 1.................... 85
Figure 57 - Measured Sa (left) and Sz (right) compared to the process parameters. 86
Figure 58 - (a) Relative density and (b) porosity measurements compared to the laser power and the energy density. 87
Figure 59 - Images of the cross-section of the samples with the respective processing conditions. 88
Figure 60 - Porosity variation through the specimen for E_d = 20 J/mm^3...... 90
Figure 61 - Porosity variation through the specimen for E_d = 25 J/mm^3...... 90
Figure 62 - Porosity variation through the specimen for E_d = 35 J/mm^3...... 91
Figure 63 - Microscope images of the cross-section of the samples. 92
Figure 64 - Micrography of the samples with (a) P = 150 W and Ed = 20 J/mm^3 and (b) P = 240 W and Ed = 35 J/mm^3. 92
Figure 65 - Microhardness of the samples compared to the laser power and of the energy density. 93

List of tables

Table 1 - Advantages and limitations of the experimental and numerical approach.. 6
Table 2 - Experimental plan of the spreading experiments. 14
Table 3 - Results of the PSD analysis for the "good grade" sample. 22
Table 4 - Material properties used in the simulation. 29
Table 5 - Characteristic dimensions of the computational domain............. 36
Table 6 - Combination of input parameters resulting from the LHS. 60
Table 7 - Chemical composition of AlSi10Mg powder. 76
Table 8 - Experimental processing conditions. 81
Table 9 - Comparison of SLMed Al-Cu-Mg alloys process parameters and properties as found in the literature. 97

Abstract

The term Additive manufacturing refers to a wide family of production technologies that can be classified based on a great number of features such as the operating principle and the material employed however, this thesis will focus on the Laser Powder Bed Fusion (LPBF) technologies and more specifically on the powder bed deposition stage. LPBF technologies (AM) have become commonly used method for the production of parts to be employed in critical applications in an ever-expanding list of fields ranging from aerospace and automotive to medical devices [1]. Indeed, the popularity of this method of production resides in the undeniable advantages it allows, i.e., material savings, design flexibility, customization etc. and in how such advantageous features perfectly apply to cases where a complex design and reliable mechanical properties are required for small batches productions. However, a further affirmation of LPBF technologies is hindered by the incomplete understanding of the complex multiphysics involved. Indeed, the selection of the operating process parameters is not trivial in case of novel materials and requires a laborious trial and error approach that can in turn lessen, if not completely even out the aforementioned advantages. Another weakness of this technologies is the high volatility of the finished parts characteristics if compared with more traditional and stable methods that leads to issues such as process repeatability, internal defects of the printed parts, and non-uniformity of the properties within the building chamber[2]. In fact, a Laser Powder Bed Fusion process comprises multiple stages: first, the feedstock material, in the form of micrometric powders, is spread in layers ranging from few microns to several dozens, then selected areas of the deposited layer are melted by a focused laser beam. The steps are repeated until the final part is completed [3]. As mentioned before the work presented in this

thesis will focus on the first step: the powder bed deposition. This step can be regarded as a sub process with his own input parameters and outputs which in turn can influence the successive step and the printing process as a whole. Indeed, the spreading process is the only form of control over the state of the powder bed that will be processed by the laser beam and any defect or discontinuity will affect the layer and consequently the final part. Moreover, the laser's parameters (i.e., power, scan speed etc.) are set not taking into consideration the local variations in the powder bed characteristics and are unlikely to be ideal for the whole layer. Therefore, clarifying the relationship that links inputs and outputs means being able to obtain the desired characteristics of the powder bed trough an appropriate selection of the process parameters and ultimately grants more control over the final result. Such a fine level of control on the process has significant implications on both industrial and research applications. From the industrial point of view, it means increasing the reliability of the existing process, eliminating probable sources of defects, obtaining more uniform mechanical properties throughout the printing chamber and between successive prints. Moreover, the characteristics of the powder bed could be chosen as to enhance the laser-matter interaction, increasing the energy efficiency of the process. As for the research on the topic, clarifying and controlling the spreading mechanisms is pivotal in cases where the feedstock material is made up of particles with significantly heterogeneous characteristics (e.g., size, material, shape etc.) in order to avoid segregation phenomena or suboptimal spreading that can cause defects in the final part. This scenario is relevant when dealing with the printing of tailored materials or new alloys. In this light, the extent of the impact of a complete comprehension of the link between the spreading process parameter and the resulting powder bed appears evident. Therefore, the aim of this thesis is to investigate the powder bed deposition stage during a LPBF in order to deepen the understanding the spreading mechanism. The investigations have been carried out by means of both a numerical and experimental approach. The outline is the following:

- Section 1: State of the art
- Section 2: Experimental analysis
- Section 3: Numerical model
- Section 4: Application
- Section 5: Future developments
- Section 6: Conclusions

Section 1: State of the art

In the last decade LPBF processes, along with all the other Additive Manufacturing technologies has received a lot of attention from the academic community leading to the formation of an extensive literature on the topic, based on both experiments and numerical simulations. This literature is mainly focused on the laser processing stage with many studies analysing the molten pool formation as well as the solidification and microstructure evolution [4] and dealing with the proper selection of the parameters, e.g., hatch spacing, beam power, scan speed[5]. Nie *et al.* [6] examined the scan speed effect on single tracks and the overlapping effect on multitrack parts of Al-Cu-Mg alloys. The energy density was related to the melting pool width and a 65% overlap and 10 m/min scanning speed to the higher density of the samples and no cracks. Wang *et al.* [4] studied a SLMed Al-3.5Cu1.5 Mg-1Si alloy analysing both the microstructure and the mechanical properties, finding the maximum densification for a laser energy density of 182 J/mm3. Della Gatta *et al.* [7] focused on identifying the process parameters for a customized Al-Cu-Mg-Si alloy and were able to obtain a maximum relative density of 97%, pointing out a predominant role of the laser beam power. However, similarly to the cited works, in most of the literature on the topic the characteristics of the underlying powder bed are often assumed and not derived from the real processing conditions, if not completely neglected. However, the laser-matter interaction is strongly influenced by the properties of the underlying powder layer, such as the particle size distribution, surface topology, and packing factor [8], [9] which are in turn determined by the feedstock material and the spreading process parameters [10]. This omission could undermine the results that were obtained. Due to the unidentified spreading mechanism, which may result in significant differences in the morphology of the powder layer, the observed "optimum" cannot be immediately translated to any printing procedure. These characteristics can also drastically vary within the same layer and between layers at the same position in the powder bed. Therefore, if a specific state of the powder bed was taken into account when optimizing the laser processing parameters, the aforementioned variations could result in less-than-ideal laser-matter interaction, which would lower the quality of the printed parts and eventually lead to defects like lack of fusion (LOF) or porosities [11].

For these reasons, in the latest years, the researchers have focused more on powder bed deposition stage. After a deep survey of the literature on the topic it is possible to identify two different approaches to the problem, with their unique advantages and limitations: Experiments and numerical simulations.

The experiments are conducted on different machines with varying degrees of fidelity to the actual process, ranging from the freehand layering of powders with dedicated setups to the use of specially sensorised actual 3D printers, based on the purpose of the research activity. Many researchers have applied different classes of optical measurement methods such as structured light [12], low coherence scanning interferometry [13], or fringe projection profilometry [14] to acquire the surface of the spread layer during the printing process, applying artificial intelligence to identify and correct macroscopic defects in the powder bed before the laser processing stage, leading to an effective form of online control. However, some form type of sampling is required in order to acquire more essential aspects of the powder bed, such as the packing factor and local size distribution. A strategy was developed by Ali et al. [15] that involved sampling portions of the powder bed with a UV curable polymer and analysing the samples using nano-computing tomography (CT). Other researchers developed and 3D-printed a hollow component that served as a container for the powders, which were later retrieved and weighed to measure the regional packing density [16]. A common approach also requires the use of simple setups that sacrifice the fidelity and precision of the process to enhance the observability of the results. Ahmed et al. used a makeshift cardboard stencil (25 mm × 2.5 mm) with two glass slides and manually spread a thin layer of powder, to be able to observe it under a microscope [17]. As showed, an experimental approach can convey useful information on various aspects of the spreading process, however, it also has some drawbacks. First, due to the small length scale of the particles it is difficult to characterize the process on a particle scale. Indeed, there is no universally recognised strategy for the analysis of the powder bed, therefore the data that can be extrapolated from the literature on the topic are scattered and do not follow an organized structure. Moreover, the setups required to perform the experiments can be costly and time-consuming, considering the additional design burdens. The same applies when using an actual 3D printer, considering the downtime of the machine. Alternatively, simple setups can be used but the loss in fidelity and reproducibility cannot be ignored. The use of numerical simulations enables a deeper comprehension of the complex spreading mechanisms at a particles scale, while allowing for more flexibility in the parameter' selection. The behaviour of the particles can be analysed based on every different characteristic (i.e., diameter, material, shape etc.) of the latter and under various processing condition (i.e., layer thickness, spreading speed, geometry of the recoater) with simple changes to the source code. Almost the entirety of the works in the literature makes use of the Discrete Element Method (DEM), first proposed by Cundall and Strack [18]. The DEM tracks the time evolution of each particle independently, in a Lagrangian fashion, based on the forces applied to the particles by an external source or by other particles, and updating his position and velocity after a fixed amount of time. A more detailed explanation on how the numerical method works will be presented in a later section. DEM based models have been successfully used in the simulation of granular systems [19] and suspensions [20] and have been proven to be suitable to accurately predict the powder spreading in Laser Powder Bed Fusion (LPBF) techniques. Parteli and Poschel [21] developed a numerical tool that explicitly takes into account the complex shape of the particles and used it to investigate the effect of a varying coating speed and particle size distribution on the surface roughness. Moreover, the load on the partially built part was also monitored. Mindt et al. [22] focused on the spreading of commercial Ti-6Al-4V powder, comparing the results with that of simpler 'rain' models. The effect of the coating speed and building plate displacement on the powder packing density was investigated. In the work from Haeri et al. [23], the focus was on how different aspect ratios of the particles influence the roughness and the solid volume fraction of the powder bed, showing that optimal results can be achieved for an aspect ratio of 1.5. It was also shown that a roller performs better than a blade in terms of geometry of the spreading device. These findings are qualitatively confirmed by experiments, even though the experimental setup does not realistically reproduce the spreading conditions. Chen et al. [24]developed a numerical model to investigate the powder flowing behaviour, explicitly taking into account the cohesive forces between the particles. Decreasing the particle size was beneficial for the fluidity of the powder bed. However, for particles with radius lower than 21.8μm, the effect of the cohesion forces becomes prominent, hindering the powder flowability. An experimental validation was carried out, comparing the simulated and the real profile of the powder heap in front of the blade during the spreading process. Similar findings by Meier et al. [25] confirmed that if the median diameter of the particles is too small, the resulting powder bed quality can be compromised. Haeri [26]used a DEM model to identify more efficient shapes for the spreading device that can lead to a quasi-critical value of powder bed density. Nan et al. [27] studied the jamming caused by the highly frictional nature of the powders used in AM. The frequency and duration of the jamming phenomena were related to the layer thickness. Zhang et al. [28] employed a DEM model to simulate ceramic powder roller-spreading with specific attention to the influence of the layer thickness and of the roller parameters on the packing factor of the powder bed. Chen et al. [18] focused on the deposition mechanism at a particulate scale and tried to establish a comprehensive model. Three competing mechanisms which can influence the packing density of the powder bed were identified: the cohesion effect, the wall effect, and the percolation effect. A similar approach can be found in Fouda et al. [29], showing that the final deposited layer packing fraction is influenced by the dilation caused by the starting of the spreader, the rearrangement due to the crossing of the gap, and the inertia of the already deposited particles. Furthermore, the relationship between the process parameters and the relative influence of those mechanisms was also highlighted. Han et al. [30] tried to establish a systematic approach for the optimization of the layer thickness. A numerical model was developed to analyse the effect of the layer thickness on the powder bed density and the optimum parameters were used to produce samples whose microstructure and tensile strength were assessed. Desai et al. [31] employed an interesting approach to overcome the limitation of the high computational power required by DEM method by using the DEM-based simulations to train a feed forward, back propagation neural network which was then used to study the relationship between spreading parameters and process results. However, some limitations exist when using a DEM based numerical model. Indeed, these models do not scale well with the number of particles in term of computational power required, therefore only a limited part of the whole process can be reproduced. Moreover, the selection of the parameters for the DEM model usually requires complex calibration procedures. Another strong limitation is represented from the shape of the particles. Complex shapes can be modelled to some extent with overlapping clusters of spheres, at the cost of additional computational power requirements. It is also worth mentioning that, given the scarcity and fragmentary nature of experimental data, most of the cited works are totally not validated with some having just a partial validation of the results. The main advantages and limitations of the two approaches are summarised in Table 1.

Table 1 - Advantages and limitations of the experimental and numerical approach.

Experimental		**Numerical**	
Advantages	Disadvantages	Advantages	Disadvantages
Full scale	Costly	Particle scale	Computationally demanding
Trustworthy	Limited number of parameters to explore	Flexibility in the setup and parameter selection	Simplifications are required
			Hard to validate

The fragmentary nature of available data also applies to studies that make use of numerical models to investigate the powder bed deposition. Indeed, the presented results are often only valid if referred to the same material, with the same parameters and the same setup for the process. However, in many studies it is possible to identify common results that can be summarised as follows:

- Spreading speed can influence the characteristics of the deposited layer.
- Due to the size of the metallic powders commonly used as feedstock material, the adhesive effects play a crucial role and should therefore be taken into consideration, both during the modelling and when selecting the material for real printing processes.
- The layer thickness should be selected carefully since an improper selection can lead to detrimental effects.
- The effective layer thickness may deviate significantly from the nominal, usually increasing for the first few layers up to a stable value.
- The characteristics of the powder bed can vary significantly in the direction of advancement of the recoater.

Regardless of the method used, there is still need for further analysis. Indeed, a proper comprehension and optimization of the spreading process is far from be achieved. The works in the literature do not address what happens in the layers after the first and at the same way ignore the recursive nature of the process, where the result of the previous layer influences the successive spreading.

Section 2: Experimental analysis

2.1 Materials and methodology

The next section will cover the experimental part of this thesis, describing in due detail the equipment, the selected feedstock material as well as the experimental procedure followed. The assumptions and underlying motivations as well as the results will be presented and discussed.

2.1.1 The experimental device

The spreading process tests that will be discussed later were performed on the specially constructed apparatus in Figure 1 that accurately mimics the layering apparatus of a commercial 3D printer.

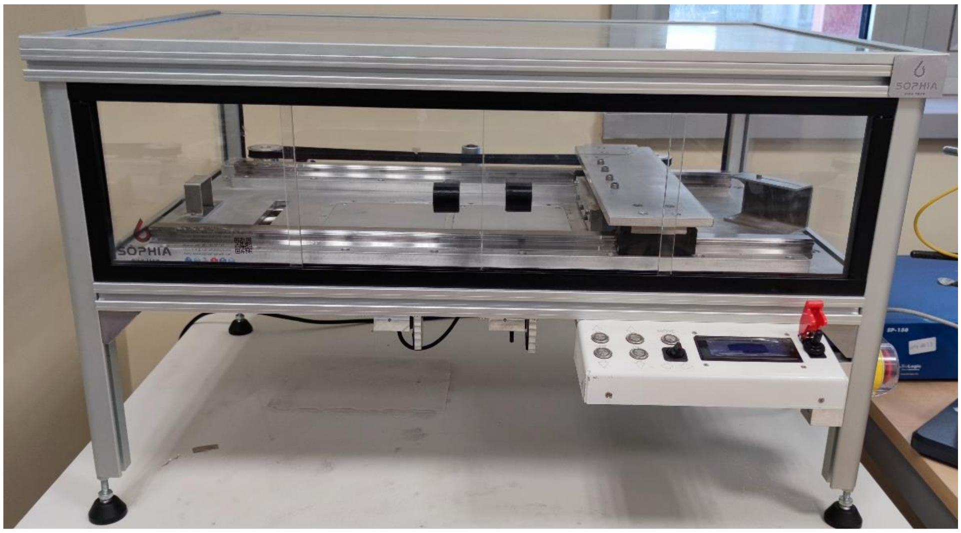

Figure 1 - Experimental device used in the spreading experiments.

Due to a number of benefits, such as unrestricted access to the powder bed without being constrained by the additional equipment of a real 3D printer, the freedom to operate and modify the device itself, and a large selection of process parameters, an independent open architecture device was preferred. Nonetheless, the level of precision required to guarantee the correct conduction of the process is met, ensuring stable and reproducible results. Both the feedstock and deposition plate measure 150x150 mm and can be vertically adjusted via two independent micrometric screws. The vertical offset of the deposition plate after each pass of the recoater defines the layer thickness, while the overall amount of powder that is deposited for each layer can be controlled by moving the feeding plate. In a perfect world, the amount of powder removed from the powder feedstock would match the amount of powder deposited in each layer. However, due to a less than ideal spreading procedure, it is typically raised to prevent subpar layering or feeding errors. The surplus powder is collected for further reuse in a tank at the end of the deposition zone. In order to avoid complicating the experimental setup with other variables a simple vertical rubber blade was preferred to a more complex device, such as a roller or similar.

2.1.2 The feedstock materials

As for the feedstock material, Al powders, which will be referred to as "poor grade," and IN718 powders, which will be referred to as "good grade" were the two materials taken into consideration. The term "poor grade" refers to some characteristics of this powder, such as an uncontrolled aspect ratio, a lack of sphericity, and a relatively wide range of particle sizes, which make them unsuitable for additive manufacturing. These characteristics are evident in

Figure 2, which displays an image of Al powder taken with a scanning electron microscope (SEM, Hitachi TM 3000).

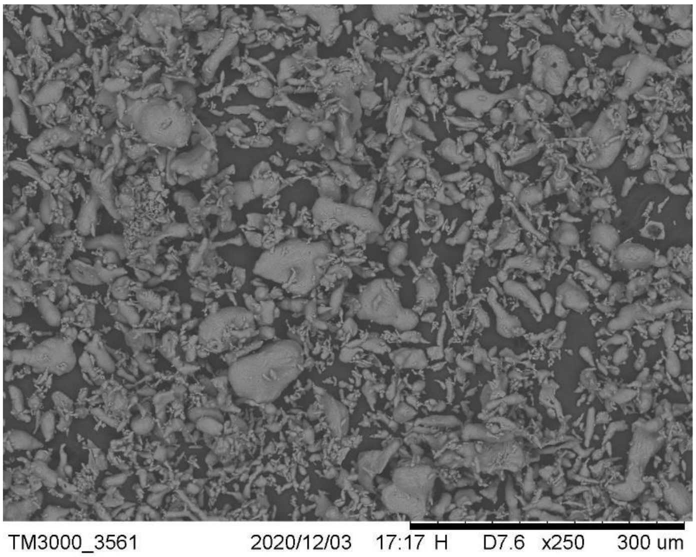

Figure 2 - SEM image of the “poor grade” feedstock material.

On the other hand, as can be seen from Figure 3, the "high quality" sample of IN718 (= 8.19 g/cm^3) is made of particles that have a better degree of sphericity and a more regulated aspect ratio. Additionally, the PSD chart demonstrates that the particle diameter has a reasonably flat slope and ranges between 10 and 50 µm. These two fairly dissimilar feedstock materials were selected to try to highlight any cross correlation between the process parameters and the characteristics of the powders.

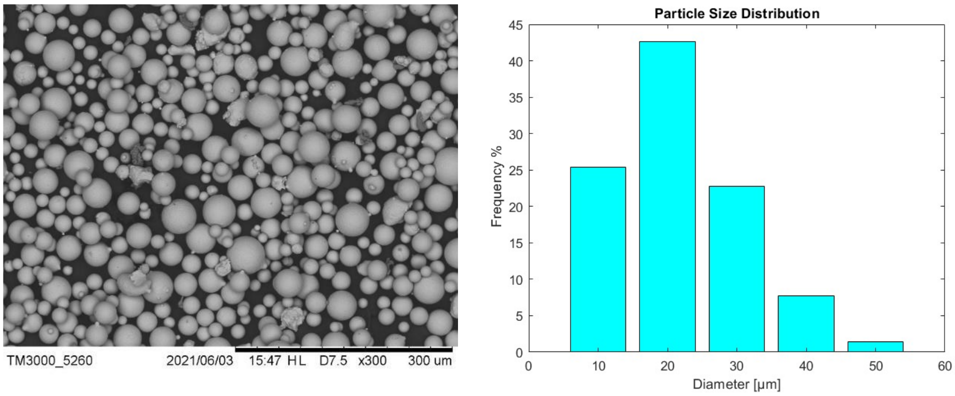

Figure 3 - (Left) SEM image of the "good grade" feedstock material. (Right) Particle Size Distribution of the "good grade" material.

2.1.3 Powder bed characterization

As mentioned before, the powder deposition stage can be regarded as a sub process per se, with his own process parameters and target outputs. Specifically, in this thesis the process parameters chosen are the layer thickness and the spreading speed, along with the two different feedstocks presented earlier. The target output chosen to evaluate the deposited powder bed are the packing density, the surface characteristics of the top layer and the particles size distribution. Instead of focusing just on an average value of the powder bed features, we have assessed the properties at various points in the powder bed to pinpoint areas where the deposition outcomes may be less than ideal or significantly different, as well as the potential for segregation phenomena. Indeed, besides having good characteristics of the powder bed it is preferable for them to be distributed uniformly on the deposition plate. In this light, the four corners of the deposition plate, as shown in Figure 4, were the four locations where the powder bed was examined. To reduce their impact, each sampling spot is 30x30 mm in size and placed 20 mm from the edges of the deposition plate.

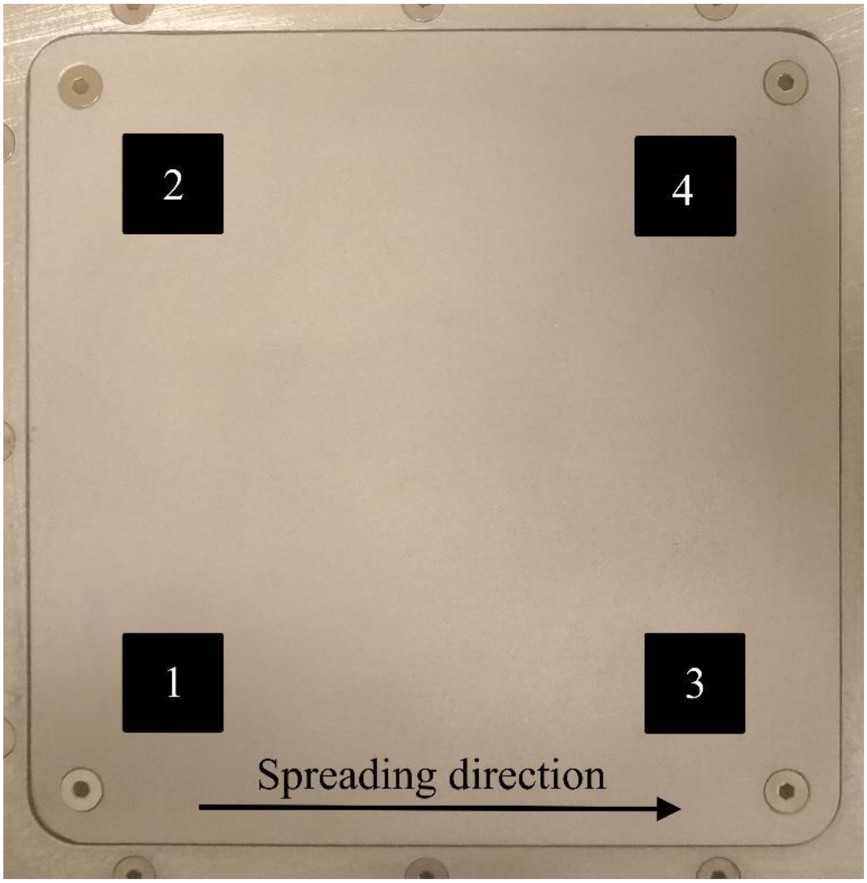

Figure 4 - Position of the sampling zones in the deposition plate.

There are no additional stages of compaction in an additive manufacturing process, therefore the spreading process is the only one that can affect the packing density of the powder bed. In our studies, a known-volume portion of the powder bed was removed using a special instrument made to retrieve a sample from a shallow powder bed. The sample was weighed using a precision balance to determine the powder bed's local packing density. The topology of the powder bed surface in its loose state as a result of the spreading process has a direct impact on the laser-matter interaction and, subsequently, on the effectiveness of the heat transfer mechanisms. This is especially true for reflective materials, for which the main mechanism of absorption is multiple refraction between powder particles [32]. Given the loose nature of the powder bed's surface, in-situ observation is the only way to describe it. Specific spots with an extension of around 1 mm2 were observed with the use of a Wi-Fi microscope mounted on a specifically designed platform. To measure the quality of the deposited powder bed, the instrument's restricted depth of focus was exploited. The strategy described above was used to characterize the powder bed obtained used the experimental device presented above. More specifically, 30, 50, and 100 µm were chosen as the three levels of layer thickness. Although a layer thickness of 100 µm is primarily used for technologies like electron beam melting, where the use of a different heat source (namely an electron beam) with more penetrative potential allows for the deposition of thicker layers of powders [33], these values are within the typical ranges used in LPBF applications [34]. However, prior studies have shown that the thermal contraction of the previously printed part during the printing process can cause the real thickness of the layer of powders to differ, sometimes significantly, from the nominal one [35]. This led to the inclusion of a layer thickness of 100 µm in the study. Two levels of the recoating device's speed, 30 mm/s and 60 mm/s, which lie within the scope of usual AM applications, were taken into consideration. Additionally, a lesser spreading speed of 10 mm/s was also used as a benchmark. The very low spreading speed can have a substantial impact on the overall process time and is of little industrial importance because recoating occurs at every layer. As a result, only one iteration was performed. Based on the aforementioned factors, Table 2 reports the experimental strategy that was produced, which included a total of 7 unique combinations for the two feedstock materials. Multiple layers were deposited for each set of parameters, and the powder bed was then characterized.

Table 2 - Experimental plan of the spreading experiments.

Experiment	Sample	Recoating speed [mm/s]	Layer thickness [μm]
1	Poor grade	60	100
2	Poor grade	60	50
3	Poor grade	60	30
4	Poor grade	30	100
5	Poor grade	30	50
6	Poor grade	30	30
7	Poor grade	10	100
8	Good grade	60	100
9	Good grade	60	50
10	Good grade	60	30
11	Good grade	30	100
12	Good grade	30	50
13	Good grade	30	30
14	Good grade	10	100

2.2 Results

This section will present the results of the spreading experiments, along with a discussion of the probable causes for these results. Understanding the probable reason of these variances is crucial to achieving a more stable process and fully realizing the potential of these technologies, considering the crucial role the powder bed plays in an LPBF. This further supports the reasoning behind the work and the need to have a solid investigational methodology to define the spreading stage of the process. It should be pointed out that the results produced by the adopted method do not adequately account for either the unique contribution of each layer or any variation in the effective layer thickness. Nevertheless, the current results provide useful information.

2.2.1 Poor grade feedstock material

First, the focus will be on the results with the “poor grade” feedstock material. It should be noted that, the measurements are grouped and referred to as "rear" and "front" with respect to the powder bed because there is no discernible variation between zones "1" and "2," and zones "3" and "4", respectively (see Figure 4), i.e., no source of variability is found in the direction orthogonal to the spreader advancement. For the spreading experiments carried out with the "poor grade" feedstock material, Figure 5 trough Figure 7 display the relative density (i.e., the density of the measured sample normalized with respect to that of bulk aluminium). The relative density ranges from 0.25 and roughly 0.4, which is a much lower value than that found in comparable works when evaluated experimentally and numerically [10], [36]. With a thicker layer, the largest relative density is possible at the slowest spreading rate. However, with layer values of 50 µm and 30 µm, a faster spreading speed seems to be advantageous. Between the front and back sections, the relative density values are not considerably different (except for the case at 60 mm/s and a layer of 50 μm that shows a reduction of about 20%). This can be explained by taking into account the morphology and PSD of the feedstock material. in this instance, the space between the recoater and the baseplate is comparable to the diameters of the larger particles and jamming events [27] can occur, Additionally, the high velocity of the recoater fractures the interlock between the powders in the case of powders that tend to form large aggregates, allowing for enhanced flowability [37]. On the other hand, a reduced spreading speed results in a more effective deposition for a thicker layer [24]. The poor sphericity and great diversity in particle size, which might encourage phenomena like mechanical interlocking and clustering, can be used to explain the low relative density values. The cohesive effects brought on by Van Der Waals forces are relevant and aid in the development of aggregates for particles less than 100 m in diameter [25].

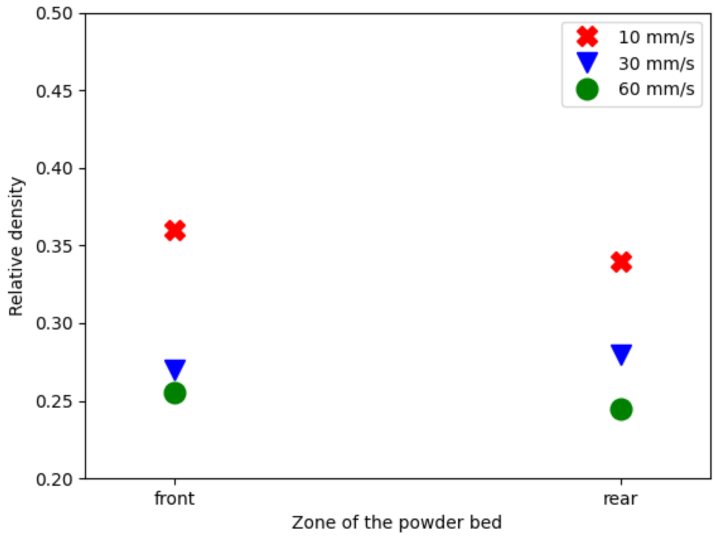

Figure 5 - Relative packing density at “rear” and “front” locations for the “poor grade" feedstock material for a layer thickness of 100 µm.

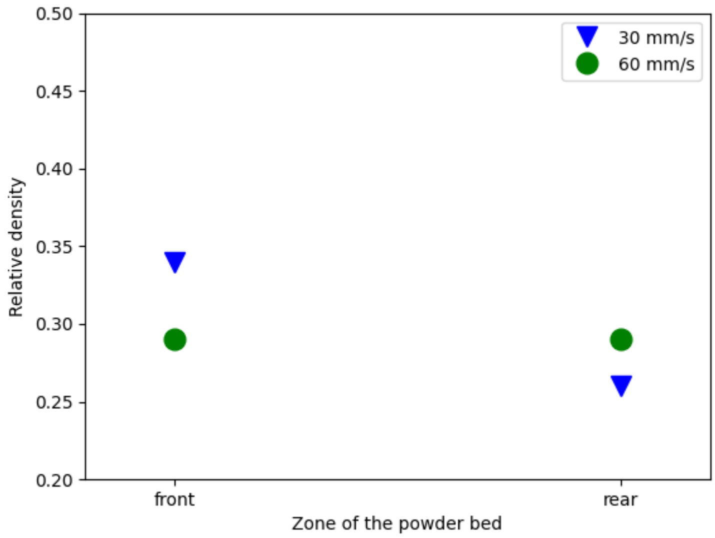

Figure 6 - Relative packing density at “rear” and “front” locations for the “poor grade" feedstock material for a layer thickness of 50 µm.

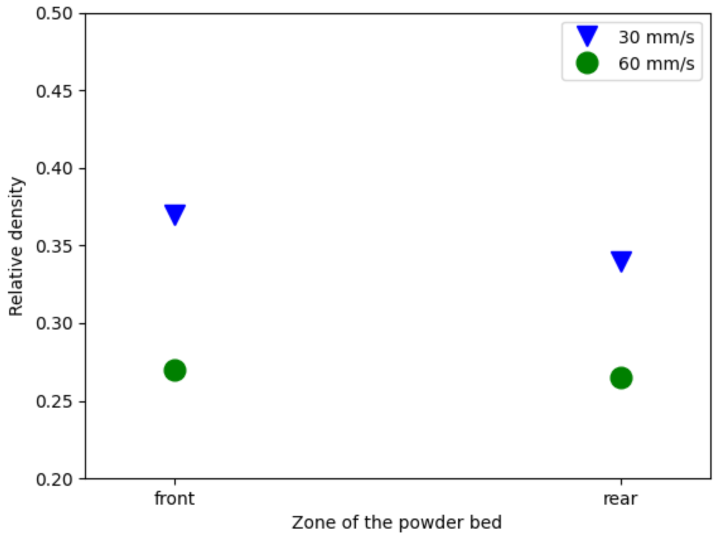

Figure 7 - Relative packing density at "rear" and "front" locations for the "poor grade" feedstock material for a layer thickness of 30 μm.

These hypotheses are strongly corroborated by the data reported in Figure 8 where the percentage of the zone that is in focus is shown. No matter where you are on the powder bed, the values for each experimental condition exhibit substantial variability (between 0.3 and 0.6). In fact, no distinct trend can be found; hence, it is difficult to see how the process parameters have an impact. The results' average low value, however, suggests that the deposited layer's surface is not uniform and exhibits intricate 3-dimensional patterns across a limited area. Since variations in substrate morphology might affect the laser absorption coefficient, the presence of these features in the top layer may be detrimental to the process's outcome. As a result, there is significant variation in the mechanical properties of the printed object because the laser-matter interaction is not uniform over the powder bed.

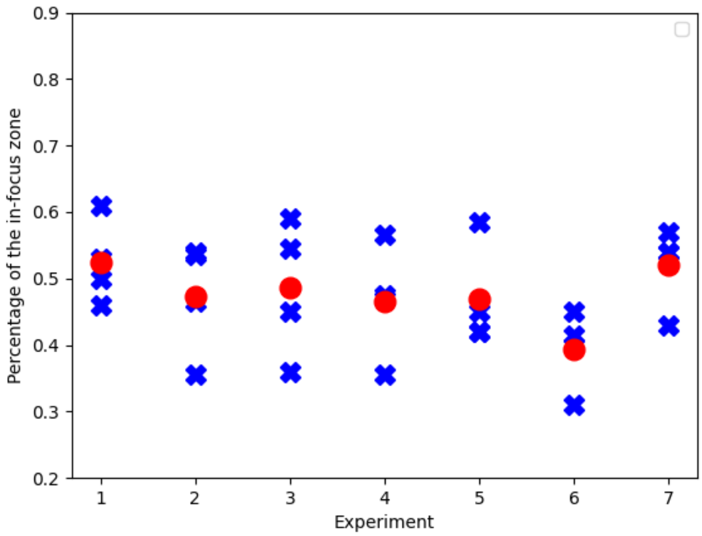

Figure 8 - Percentage of the in-focus zone for the different zones of the powder bed (blue cross) and its average value (red dot).

2.2.2 Good grade feedstock material

Following the same nomenclature for the "good grade" sample, Figure 9 trough Figure 11 depicts the relative density for various layer thicknesses and spreading speeds as a function of position on the deposition plate. For a fixed layer thickness in this situation, it is impossible to clearly identify any influence of the spreading speed. Nevertheless, it appears that the overall values, which range between 0.5 and 0.65 for all parameter combinations, are much higher than for the "poor grade" sample. Other than the relative density's variation in relation to the process parameters, there are also noticeable differences in the relative density for various spots on the powder bed.

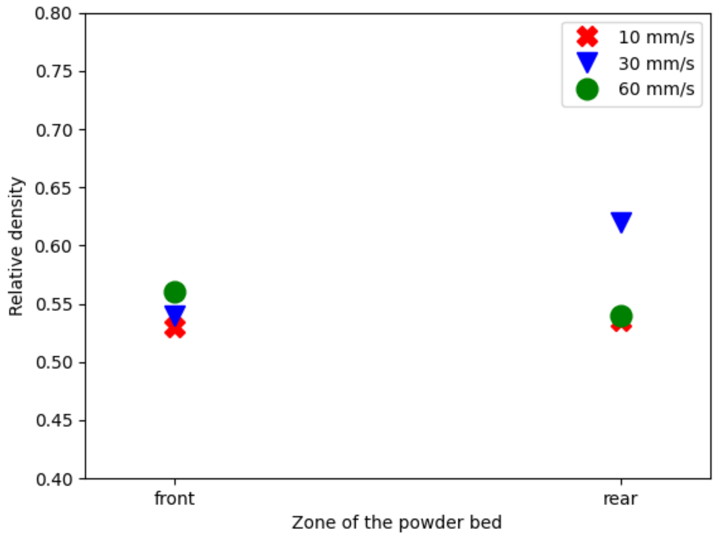

Figure 9 - Relative packing density at “rear” and “front” locations for the “good grade" feedstock material for a layer thickness of 100 µm.

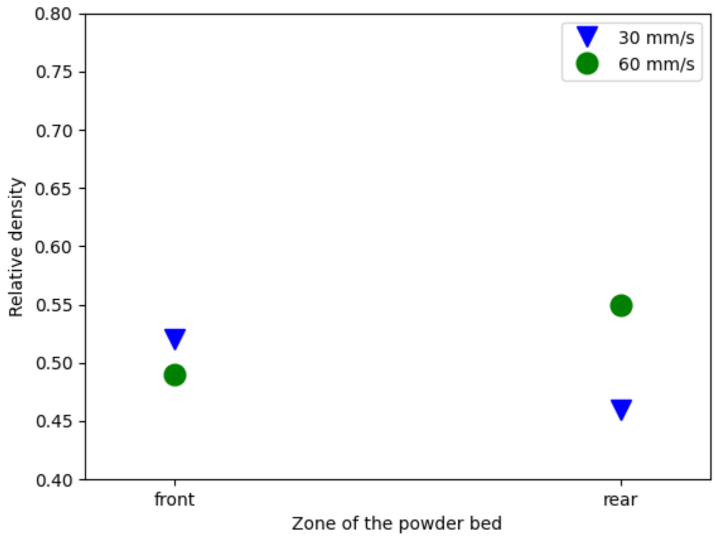

Figure 10 - Relative packing density at “rear” and “front” locations for the “good grade" feedstock material for a layer thickness of 50 µm.

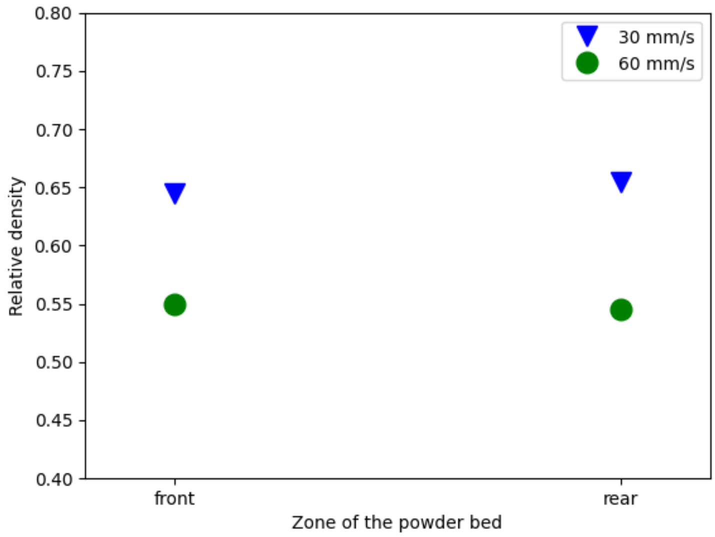

Figure 11 - Relative packing density at “rear” and “front” locations for the “good grade" feedstock material for a layer thickness of 30 µm.

Table 3 reports the findings of the analysis on the PSD of the extracted samples. Once more, because the results from zones 1 and 2 were comparable and no unexpected source of difference is anticipated, they have been pooled and given the name "rear." The zones 3 and 4 results have also been labelled as the front. Only the values of D10, D50 (which corresponds to the distribution's median), and D90 were published for the sake of clarity. These numbers represent statistical parameters that show the size of the particles that make up 10%, 50%, and 90% of the sample, respectively (ISO 9276-1:1998). The size distribution is moved toward larger diameters in comparison to the initial PSD for higher spreading speeds (experiments 8, 9, and 10), however this trend is inverted for lower spreading speeds.

Table 3 - Results of the PSD analysis for the “good grade” sample.

	front			rear		
Experiment	D10	D50	D90	D10	D50	D90
8	16.9	27.7	41.8	17.1	26.9	41.3
9	17.6	27.8	43.1	17.1	28	43.2
10	15.5	25	40.6	15.7	25.6	40.7
11	16.3	25.9	40.3	15.8	25.2	40
12	16.7	26.6	42	16.4	26.3	41.9
13	15.6	24.5	39.7	15.4	24.4	39.1
14	15.8	25.1	40.3	15.5	25.2	39.3

Due to the use of a single material and the deposition plate's tiny size in this instance, the shifting is not very noticeable, but it should be carefully taken into account when employing heterogeneous materials or when the recoater is moving in a larger range of directions. Contrary to the previous instance, the value of the in-focus zone for the high-quality sample is nearly equal to 1 regardless of the procedure settings. The features of the powder bed have significantly improved as a result of the spreading process using "good grade" feedstock. The relative packing density dramatically increases (up to 100% greater) and is on par with results from comparable works. Similar results for layer topology characterization were consistently close to one. Combining these two observations, we can infer that the sample's particle size distribution (i.e., the lack of very small particles that could be subject to strong cohesive forces and consequently form clusters) and more tightly controlled aspect ratio do not promote the negative mechanism previously mentioned, leading to a better packed powder bed. It has been noted in numerous publications in the literature [36][22] that the interaction with the recoater is what causes the volume fraction of the smaller particles to decrease from the "front" to the "rear" zone of the powder bed. If the spreading processes change as the coating speed increases, the opposite outcome can be explained. In fact, numerical studies that examined the spreading process at the particle scale have shown that the spreading speed affects the rate at which particles are deposited in the powder bed as well as the particle size (and, consequently, the inertial properties) [38], [39].

Section 3: Numerical model

This section will present the development of the DEM based model used in this thesis for the simulation of the spreading process. The numerical method will be presented in due detail, explaining the role of the parameters, the simplifications, and restrictive assumptions along with the selected calibration procedure. Finally, the results of powder bed spreading simulations will be discussed, highlighting new findings and confirmations/divergences with the mechanisms known in the literature.

3.1 The Discrete Element Method

The Discrete Element Method is an explicit numerical method, first proposed by Cundall and Strack [18], particularly suited for the simulation of the time evolution of complex granular systems. It should be pointed out that the method itself is really flexible in most of his aspects, comprising but not limited to the particles that are considered when checking for possible interactions, the degree of freedom of the particles, the presence/absence of particles belonging to the same molecule, heat transfer between particles, the selection of how the contacts are handled, however, here we will be referring to the specifics of the model used in this work. The DEM works by computing the forces exerted on each particle due to external fields (in this case only gravity) and contacts with other particles and walls. At every time step, the translational and angular velocity of the i-th particle, are obtained resolving the force (1) and torque (2) balance equations

$$m_i \frac{d\overrightarrow{u_i}}{dt} = \sum_j \overrightarrow{F_{ij}} + m_i \vec{g} \qquad (1)$$

$$I_i \frac{d\overrightarrow{\omega_i}}{dt} = \sum_j \overrightarrow{T_{ij}} \qquad (2)$$

where m_i and I_i are the particle mass and moment of inertia, F_{ij} and T_{ij} are the interaction force and torque on the i-th particle due to the other j-th particles or walls, and $\vec{g}$ the gravity vector. The torque in Eq. (2) contains a sliding component $R_iF_{ij,t}$ and a rolling contribution $\mu_rR_rk_n\delta_n$ (constant directional torque model [31]) where μ_r is the coefficient of rolling friction. The results from the previous equations are then used to update the particle position x_i and rotation angle θ_i according to:

$$\frac{d\overrightarrow{x_i}}{dt} = \overrightarrow{u_i} \qquad (3)$$

$$\frac{d\overrightarrow{\theta_i}}{dt} = \overrightarrow{\omega_i} \qquad (4)$$

The scheme in Figure 12 summarizes the various phases that take place during a timestep.

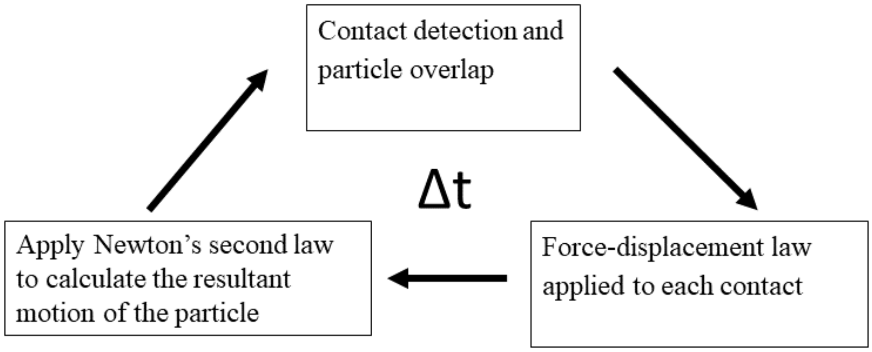

Figure 12 - Working principle of the Discrete Element Method.

Two particles are considered in contact when the distance between their centres is less than the sum of their radii, the difference between these two quantities defining the normal overlap:

$$\delta_n = R_i + R_j - \left\| x_i - x_j \right\| \tag{5}$$

The tangential overlap and the unit tangential vector are obtained from the relative velocity between the surfaces of the contacting particles. The Hertz-Mindlin contact model [40] is employed with an additional term to take into account cohesive forces, which cannot be neglected for particles smaller than 100 μm [25], as they are of the same order of magnitude of the gravity force. The normal and tangential forces acting on each particle are then:

$$F_{ij,\mathrm{n}} = k_\mathrm{n}\delta_\mathrm{n} + \gamma_\mathrm{n}\frac{d\delta_\mathrm{n}}{dt} - 4\pi \mathrm{k} R_\mathrm{r}\delta_\mathrm{n} \tag{6}$$

$$F_{ij,\mathrm{t}} = -\left(k_\mathrm{t}\delta_\mathrm{t} + \gamma_\mathrm{t}\frac{d\delta_\mathrm{t}}{dt}\right) \tag{7}$$

where k is the cohesion energy density. The tangential force obeys to the Coulomb criterion $|F_{ij,t}| \leq \mu_s |F_{ij,n}|$ with μ_s the sliding friction coefficient. The other parameters depend on the material properties trough the following equations:

$$k_{\mathrm{n}} = \frac{4}{3} E_{\mathrm{r}} \sqrt{R_{\mathrm{r}} \delta_{\mathrm{n}}} \tag{8}$$

$$\mathrm{k_t} = 8\mathrm{G_r} \sqrt{R_{\mathrm{r}} \delta_{\mathrm{n}}} \tag{9}$$

$$\gamma_{\mathrm{n}} = -2 \frac{\ln \epsilon}{\sqrt{\ln \epsilon^2 + \pi^2}} \sqrt{\frac{5}{3} m_{\mathrm{r}} E_{\mathrm{r}} \sqrt{R_{\mathrm{r}} \delta_{\mathrm{n}}}} \tag{10}$$

$$\gamma_{\mathrm{t}} = -4 \frac{\ln \epsilon}{\sqrt{\ln \epsilon^2 + \pi^2}} \sqrt{\frac{5}{3} m_{\mathrm{r}} G_{\mathrm{r}} \sqrt{R_{\mathrm{r}} \delta_{\mathrm{n}}}} \tag{11}$$

where m_r, R_r, E_r, and G_r are the equivalent mass, radius, Young's modulus, and shear modulus, and e is the coefficient of restitution. The coefficient of restitution is defined as the ratio between the kinetic energy of two objects before and after a collision and therefore, denotes how fast the energy of the system is dissipated during the impacts between particles. Some approximations are necessary in order to run simulations of a complex process (like the powder spreading in AM) in a reasonable amount of time [41]. Both the material properties (for instance, by reducing the particle stiffness [42]) and the simulation geometry can be simplified (e.g., by exploiting periodicity or simplifying the particle shape). To accurately duplicate the behaviour of the powder in real life and capture the key physical mechanism of the spreading process, the material characteristics must, of course, be calibrated. The material for the powders considered in this study is Inconel718, a Nickel-based superalloy that is largely used in AM applications [43]. More details on the reference material can be found in the previous section. Looking at the SEM images, it appears that the particles do not present any particular irregularity, therefore, in the simulations the particles will be considered perfectly spherical, thus avoiding the added complexity of a multi-sphere model. This also makes the contact resolution phase pretty straightforward. Indeed, for in case of spherical particles the contact plane (the plane which defines the direction of the normal and tangential forces) can be unambiguously identified. In case of polygonal particles, the contact plane identification can be ambiguous in case of corner-to-corner contact, requiring the definition of a contact energy function and of a strategy of minimization to find the direction of maximum gradient descent. Another key aspect when selecting the characteristics for the particles to be used in the simulation as a representation of the IN718 powders is the particles size distribution. Indeed, the particle size distribution has a relevant influence on the spreading process behaviour [44], and can influence the results of the calibration process. Therefore, in this work replicated the dispersion of a powder commonly used in AM was replicated. The experimental particle size distribution has been discretized specifically by taking into account particles of four distinct sizes, namely 13, 21, 28, and 42 μm, with number fractions of 0.2, 0.2, 0.5, and 0.1, respectively, leading to an average diameter of 25 μm. The smallest particles were truncated to produce the simulation's distribution since including them would have needed a significantly smaller time step to maintain numerical stability. An appropriate choice of timestep is crucial, since if it is too large it can lead to instabilities and consequent errors. These errors stem from the assumption adopted in DEM that the velocities of solid grains are constant within one iteration timestep. In the model adopted here the timestep was maintained lower than 15% of the Rayleigh time.

$$T_R = \frac{\pi R \sqrt{\frac{\rho}{G}}}{0.1631\nu + 0.8766} \tag{12}$$

For the same reason the Young's modulus has been reduced by several orders of magnitude. Studies have proved that such a reduction does not alter the bulk behaviour [42]. The material properties used for the model in this study are reported in Table 4 and were obtained from literature and from data available on the feedstock material. The coefficient of rolling friction is set to such a value that the rolling of a particle stops after a distance of approximately 15–20 times its radius [45]. Since the rolling friction is mostly used to account for the non-spherical shape of the powder and for the mechanical interlocking that can arise, a fine tuning of this parameter was deemed not necessary.

Table 4 - Material properties used in the simulation.

Parameter	**Symbol**	**Value**
Density [Kg/m^3]	ρ	9187
Young's modulus [GPa]	E	0.2
Poisson's ratio	ν	0.3
Coefficient of restitution	e	0.7
Coefficient of rolling friction	μ_r	0.15

3.2 Calibration procedure

The values for the remaining parameters were obtained by means of a calibration procedure. The topic of the calibration of DEM parameters has been widely explored in the literature [41], [46]–[48]. In order to guarantee a valid calibration procedure, it should be kept in mind that most of the parameters are strongly interconnected and therefore the calibration stays valid if the other conditions are the same. Moreover, one of the key problems with calibrating a DEM model is that the calibration process can consume as much computing power as the main simulation [49]. As a result, the calibration setup should be as straightforward as feasible. Specifically, in this work we will consider two target values for the comparison between experiments and simulations, namely the angle of repose (i.e., the steepest stable angle formed by a pile of powder) and the angle of slipping (i.e., the angle at which a fine layer of powder slips from a flat surface). Both these quantities have been used in the literature to characterize the flowability of bulk materials [47]. To maintain the correspondence between the number of target values and the calibrated quantities we will consider two varying parameters: the sliding friction coefficient μ_s and the cohesion energy density k. To avoid any moisture contamination of the powder to be used in the experiment for the calibration it was kept in a sealed container. The angle of repose θ_{rep} was measured by manually pouring the powder on a round-shaped base of known diameter d until it reached a maximum height h. The height of the pile was then measured, and the angle of repose was obtained as:

$$\theta_{\text{rep}} = \arctan\left(\frac{h}{d/2}\right) \tag{13}$$

The test was repeated three times and the mean value obtained for the angle of repose was determined to be about 28.7°. The other test was carried out to obtain a reference value for the slipping angle. A thin layer of powder was spread on a flat surface which was slowly tilted until the powder started slipping uniformly. At this point, the tilting was stopped, and the angle recorded. Again, the test was repeated three times and the value obtained for the slipping angle was about 41.6°. These values have been used as target values for the calibration of the DEM parameters. The simulation setup for the calibration tests faithfully reproduces the experimental one. However, to reduce the overall computational time needed to perform the calibration tests, we adopt the 'cloud method' [50] for the determination of the angle of repose: the particles are not poured through a funnel but are generated in a loose cloud above the base and let settle until a stable angle is attained. Despite the simplification, this method has shown a good accuracy and a considerable saving of computational time. While the slipping angle can be straightforwardly obtained, the calculation of the angle of repose required a post-processing strategy, since the relatively small number of powder particles in the pile leads to a rougher surface compared to the real one. As shown in Figure 13 five equally spaced points belonging to the powder surface were selected. The angle between the line that fits these points, and the horizontal plane is the angle of repose. The process is repeated for each pile along the directions shown in Figure 14 and the average of the four values is used as angle of repose.

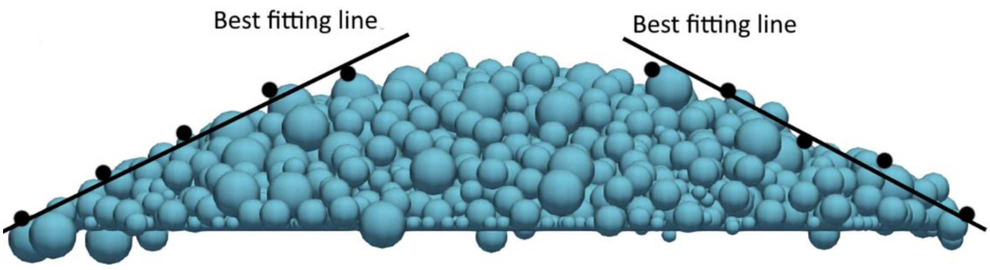

Figure 13 - Procedure for the calculation of the angle of repose.

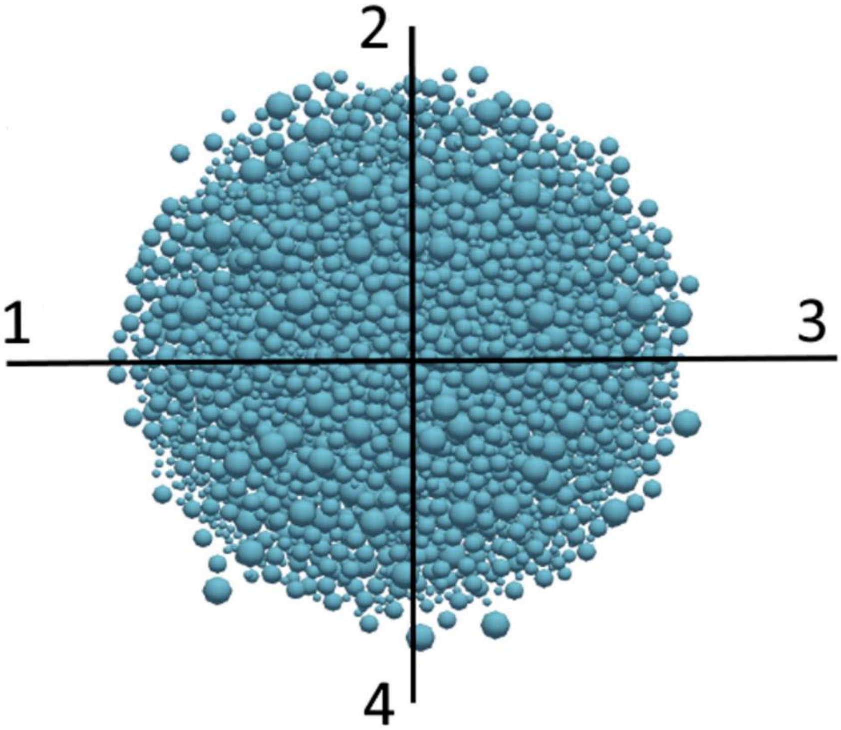

Figure 14 - Directions along which the angle of repose is calculated.

The experimental setup for the calculation of the angle of repose is presented in Figure 15.

Figure 15 - Experimental setup for the calculation of the angle of repose.

First, the parameter's space was explored running simulations with nine combinations of coefficient of friction and cohesion energy density. The value of the corresponding values of angle of repose and slipping angle were then calculated. The bounds of the parameter space were set based on the existing literature [41], [46]–[48] and on the observation of non-physical behaviour for values beyond these limits. The experimental target values are attained for the calibration parameters falling in the upper right portion of the figures. Other simulations were run with the parameters falling in this region to refine the estimate, finding μ_s = 0.7 and k = 90000 J/m^3. These values led to an error inferior to the 4 % for both the target values and were therefore considered satisfactory. An overview of this calibration procedure and its results can be found in Figure 16 and Figure 17.

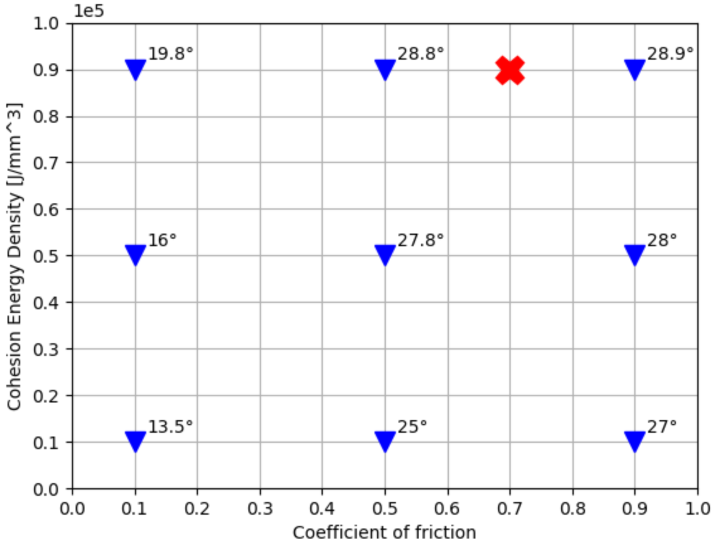

Figure 16 - Variation of the angle of repose with coefficient of friction and Cohesion Energy Density and optimal value (red cross).

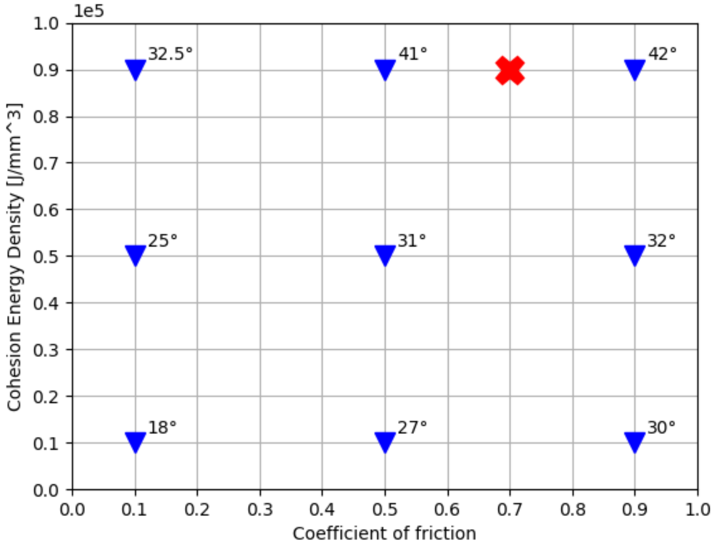

Figure 17 - Variation of the slipping angle with coefficient of friction and Cohesion Energy Density and optimal value (red cross).

3.3 Simulation setup

Once the parameters have been set the model can be used to perform a spreading process simulation. The computational domain is shown in Figure 18. It can be seen that the spreading apparatus of a real 3D printer is faithfully reproduced and both the accumulation zone, where the powder particles are gathered and build up to create a rising heap in front of the blade, and the deposition zone, where the heap is partially stratified in a thin layer, are taken into consideration.

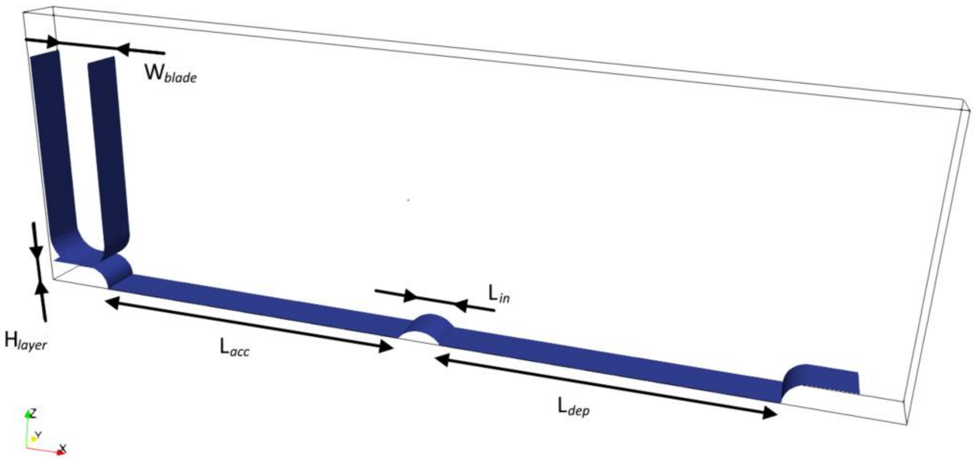

Figure 18 - Setup used for the simulations with relevant dimensions.

For the sake of reducing the computational burden of the simulations some simplifying assumptions were applied to the computational domain. First, the total extent of the zone considered in the model is significantly lower than that of a real process. It can be argued that this reduction may alter the results, however it was verified that it was the minimum distance needed to attain a steady state in the spreading process (i.e., the powder heap in front of the blade reached a constant slope, after which it started increasing in size without substantial modifications in its shape). Moreover, the domain was assumed periodic in the direction orthogonal to the movement of the blade (y-direction in Figure 18), This assumption can be found also in similar works in the literature and is reasonable since there are no sources of variation in this direction. The boundaries in the y direction were set as periodic, meaning that a particle exiting from the domain from one end is inserted in the other end with the same values for velocity and angular momentum, and with an added counter that tracks the periodic boundary the particle was first originated in. It was verified that the chosen periodic length does not alter the average results by performing simulations with increasing values of this parameter. Finally, the building plane is considered perfectly flat, while all the edges have been rounded to improve the stability of the simulation. Indeed, having a perfectly sharp edge can cause problems in the contact detection between particles and edges. The dimensions of the setup are listed in Table 5.

Table 5 - Characteristic dimensions of the computational domain.

Dimensions	**Symbol**	**Value [µm]**
Domain size in x-direction	L_x	3250
Domain size in x-direction	L_y	175
Domain size in x-direction	L_z	1125
Length of accumulation zone	L_{acc}	1250
Length of deposition zone	L_{dep}	1250
Space in between zones	L_{in}	150
Blade width	W_{blade}	250
Layer thickness	H_{layer}	100

The presented setup will be used to investigate the phenomena occurring during the accumulation and deposition phases of the spreading process and how such phenomena influence the state of the powder reservoir and the characteristics of the powder bed. The choice of parameters for the numerical simulations will not reflect that of the experiments since the heavily different length scale and, ultimately, the different scope of the two approaches would make it pointless to trivially compare the results. For this reason, the velocity of the blade is set to two values to investigate two different regimes of motion. Specifically, we set the lower value to 20mm/s, corresponding to a quasi-static regime, and the higher value to 100mm/s, where inertial effects play a significant role [25]. The other parameters are kept fixed since the main scope of the present work is to identify the underlying mechanism of the powder spreading process and not to perform a parameter optimization. Specifically, the layer was set at 100 μm as to represent a layer in a steady state.

3.4 Results

To generate the feedstock of powders for the spreading process, 4500 particles are generated above the accumulation zone and are let settle under the action of gravity until they stop moving. The quantity of powder for the feedstock is chosen to guarantee that the powder entirely covers the deposition zone at the end of the spreading process. An example of the initial powder feedstock is displayed in Figure 19. To avoid any possible influence of the initial state of the powder bed on the results, every simulation is repeated with three different starting conditions, obtained by varying the initial position of the particles. Therefore, the results will be plotted taking into consideration the mean values as well as the standard deviations (reported as error bars).

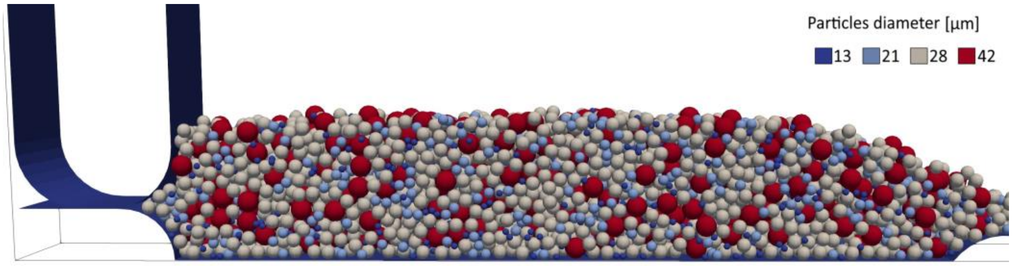

Figure 19 - State of the powder feedstock after the settling of the particles.

Two different moments can be identified when the blade start to move. First it starts accumulating particles, with the particles that move upward along the blade causing a sharp rise of the height of the powder heap. After a brief transient, the process achieves a stationary state with the powder reaching a characteristic dynamic angle of repose. The value of this angle appears to be determined by the concurrent action of two contrasting phenomena: the obstruction caused by the particles in front of the powder heap that promotes a steeper angle and the effect of gravity that causes the rolling and rearrangement of the particles in a more acute avalanche. Since the resistance of the particles in front of the blade is more relevant at higher speeds, the dynamic angle of repose increases with the velocity of the blade from around 25° to over 36° as shown in Figure 20, where the typical angle at which the particles arrange can be observed.

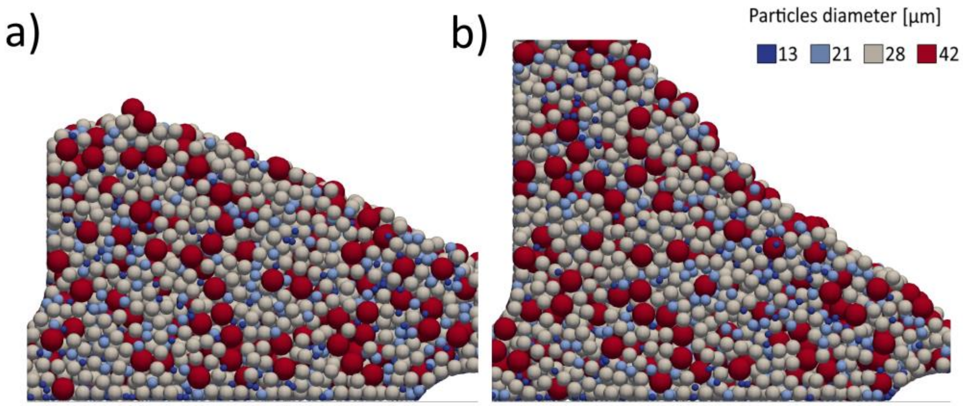

Figure 20 - Dynamic angle of repose in the accumulation stage for two different speeds of the blade: (**a**) 20mm/s, (**b**) 100mm/s.

Once the stationary state is attained, as more particles are swept, the powder heap grows without any alteration of the shape. In this state, the mechanism of the powder heap accretion can be identified. Indeed, the diameter of the particles has a considerable impact on their trajectory. The smaller particles can fill in the spaces left behind and sink into the powder reservoir with a mechanism somewhat resembling that seen in granular convection, whereas the larger ones have a tendency to become caught in the powder heap [51]. This event demonstrates the existence of vertical interactions that have the power to affect the subsequent layers' and the powder reservoir's condition. In fact, following the spreading process, the reservoir's powder's mean diameter slightly decreases from its original value of 25 µm to a value of 23 µm. Moreover, the mass of powder left in the reservoir after the spreading decreases of about 27% for the highest speed of the blade. Although this phenomenon won't have a direct impact on how the current layer is spread, it may change how much powder will be spread overall in the following layer, which could result in flaws like short feed. The behaviour of the powder heap changes once the blade reaches the deposition zone. the lack of new particles on the trajectory of the blade causes a significant reduction in the dynamic angle of repose. In addition, as shown in Figure 21, the larger particles on the free surface of the powder heap are drawn down and accumulate towards the bottom of the heap because they are more susceptible to the effects of gravity. This phenomenon causes segregation, which has an impact on the final powder bed. This build-up is more noticeable with lower blade speeds.

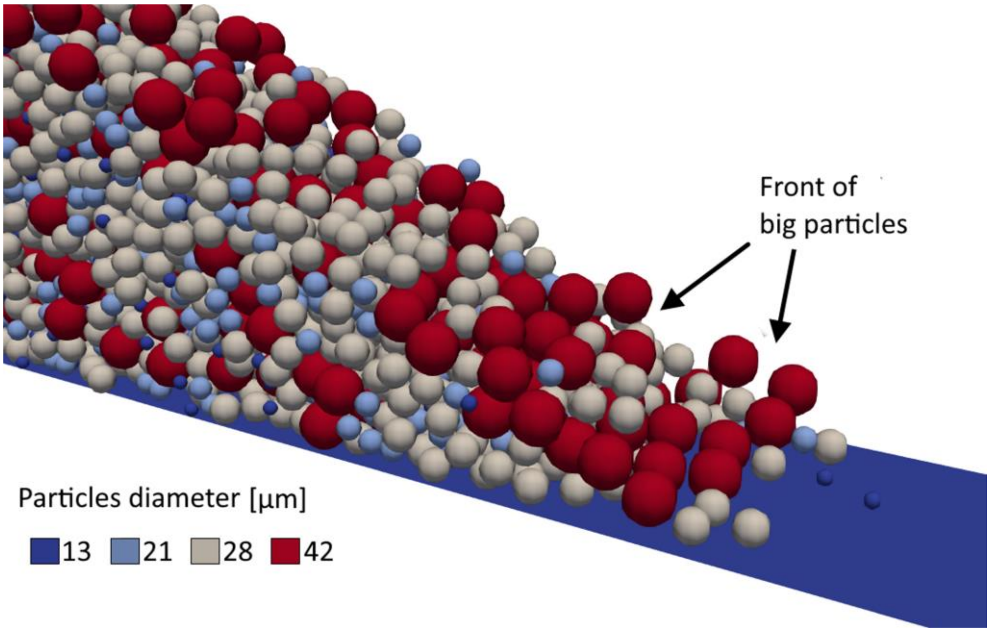

Figure 21 - Snapshot of the base of the powder heap, where a front formed by the bigger particles can be observed. The picture is referred to a 20mm/s spreading speed.

The powder bed is divided into 15 evenly spaced sub-regions along the spreading direction in order to quantitatively evaluate its condition following the spreading operation. In each zone, the relative density, the effective layer thickness, and the mean diameter along the spreading direction are calculated. The top border of the particles that are on the powder pile's surface are measured along the z-axis to determine the effective layer thickness. The volume of the theoretical layer divided by the total mass of the particles yields the relative density, which is then normalized using the bulk material's density. The height of the effective layer thickness, the width of the simulation box, and the length of the sub-region are used to compute the volume of the theoretical layer as well as the volume of the rectangular parallelepiped. The average diameter of the particles having centres within a sub-region is the mean diameter. Figure 22 depicts, for the higher and lower blade speeds, the status of the powder bed (panels a and b) and the three aforementioned values along the spreading direction (panels c to e). It can be assumed that the particles have a velocity in the spreading direction that is a portion of the speed of the blade itself since the re-coating device interacts with the particles.

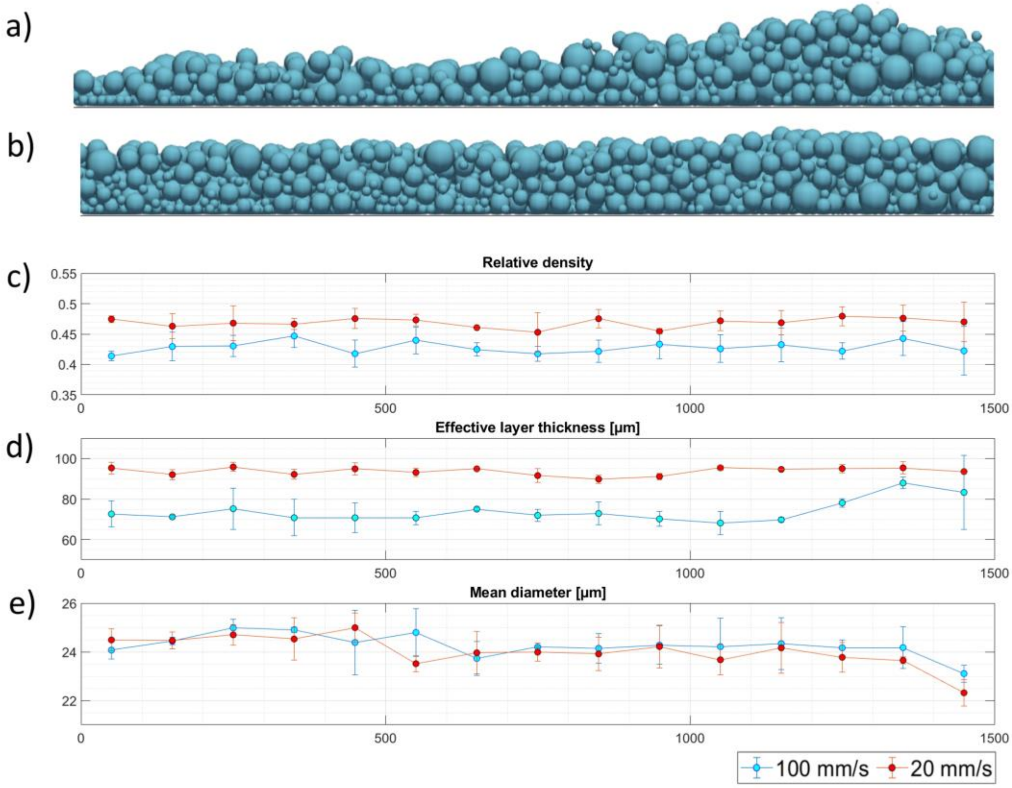

Figure 22 - Typical state of the powder bed after the spreading process at (a) 100mm/s and (b) 20mm/s. (c) Relative density, (d) effective thickness, and (e) mean diameter of the layer of powder along the spreading direction.

As a result, in the high-speed case, a void can be seen to form in the powder bed's beginning region where the effective layer thickness is much lower than the gap size (100 μm), while the particles also tend to collect in the powder bed's ending region where the effective layer thickness increases noticeably. The movement of the blade has a significant impact on how these discontinuities arise (a similar pattern is seen in reference [25]). Towards the end of the deposition zone an increased variability can be observed in the relative density. More particularly, the ‘rebound effect' [30] that takes place with smaller values of the layer thickness and the aforementioned particle segregation can both be linked to this phenomenon. The wall at the end of the deposition zone, which is a solid impediment, interferes with the blade's trajectory and causes the rebound effect. The particles captured in between give rise to force arcs as the blade approaches the obstacle. When these force arcs break due to blade movement, the particles are discharged at a relatively high speed and change the composition of the deposited bed. It could be argued that the impact of such phenomenon should be negligible because it takes place in a small region at the end of the powder bed that is not used for actual print processes, the results hint that a similar mechanism could somehow come into play any time there is an interaction between the loose powder and a solid object (i.e., the already printed part Apart from these zones, a slower spreading speed leads to a more stable layer thickness and to a larger relative density, leading to a higher quality of the powder bed. From Figure 22 panel e, it can be seen that the mean diameter of the powder reduces throughout the powder bed, further confirming the arise of segregation phenomena, similarly to what was observed in the accumulation stage. The reduction of the mean diameter in the initial portion of the powder bed observed can be explained noting that the biggest particles have a bigger momentum when dragged by the blade therefore move farther in the spreading direction and for higher speeds of the blade this appears to be slightly more evident. However, in the rest of the powder bed, at variance with what was observed for the effective layer thickness and the relative density, a lower spreading speed promotes the aforementioned segregation phenomena, thus leading to a more stable trend that results in a variation of the size distribution throughout the powder bed. More specifically, the mean diameter constantly decreases alongside the spreading direction, since the big particles accumulated at the base of the powder heap are deposited first, leaving an overall finer powder for the remaining part.

3.4 Parallelization

The presented numerical model provides useful insights on the physical mechanisms taking place during the spreading process and can be used as a starting point to properly set the parameters of the spreading process and design novel printing machines to improve the quality of the spread powder and of the resulting printed part. the trends identified have been discussed, identifying the underlying physical reason and are also consistent with those found in the literature on the topic further confirming the reliability of the model. However, while all of the above holds true, the limitations and simplifications of the model are undeniable and while some (i.e., the reduction of the stiffness) have been proven to not alter the results, other (i.e., the limited extension of the computational domain and only simulating the first layer) should be removed in order to obtain a more truthful description of the process and to uncover the inner workings that remain hidden due to the above simplifications. It should be noted that the computational domain has been scaled down mainly to avoid excessive running time of the simulations therefore the first and most immediate solution to increase the complexity of the model without impacting the running time is to increase the computational power dedicated to performing the calculations. This result can be achieved via parallelization i.e., the distribution of the computational load on several processors. The open-source software package on which the simulations presented in this work of thesis is LIGGGHTS [52], a fork of LAMMPS [53], with the addition of mesh geometry support, granular models for particle–

particle and particle–wall interactions, and particle–particle and particle–wall heat transfer. Due to the common basis, LIGGGHTS natively supports the use in a parallel environment via message passing interface (MPI). Static domain decomposition performs relatively well in homogeneous condensed matter simulations, however in typical DEM applications, specifically in our case, the distribution of the particles is widely inhomogeneous and time varying which can lead to performance limiting load imbalances. Therefore, the implementation of a dynamic domain decomposition is needed. As a result, the computational domain is split into a cartesian grid of subdomains that can be mapped to MPI processes. The user can specify how many subdomains must be created in the x, y and z directions. Each subprocess is responsible for the calculations regarding the particles inside the respective subdomain and an additional distance, whose extension depends on the biggest particle radius. The particles that belong to this region are branded as “ghost atoms” and their information (i.e., radius, position, velocity) are synced from the subprocess that owns the particles. Starting from this initial decomposition the imbalance is calculated as the maximum number of particles belonging to a subprocess divided by the total number of particles. When this number is too high a new domain decomposition takes place. Using a recursive multi-sectioning approach, slices are enlarged by modifying the borders of the slices. The method interpolates new split sites such that each slice might include the appropriate amount of particles based on the previous split locations and the aggregated total of particles up to these points. The quality of the new decomposition is assessed after computing the actual number of particles in the new slices across all processors using these new divides. This is continued until either the maximum number of tries has been made or the required particle distribution has been achieved by a reasonable margin. This should in theory guarantee that the workload is evenly distributed among the subprocesses with the maximum speedup attainable. However, it is not always trivial to obtain a substantial increase in the performances when increasing the number of computational resources dedicated to a simulation.

This issue can be easily understood looking at the scheme in Figure 23 that shows a complete breakdown of the various phases of a timestep. Specifically:

- Pair time: Time devoted to particle-particle force calculation.
- Neighbouring time: Time devoted to the construction of neighbour lists for the particles.
- Communication time: Time devoted to MPI communication.
- Output time: Time devoted to writing the data on disk.
- Other time: All of the remaining time between the end of the current timestep and the beginning of the next.

These statistics are provided by LIGGGHTS itself and are obtained as the mean of the corresponding time between all of the MPI processes. An imbalance factor, calculated as the ratio between the max time for all of the MPI processes and the mean time, is also provided. Any load imbalance causes the faster processor to wait for the slower one, resulting in an overall worse parallelization. Indeed, there exist some geometries for which a proper domain decomposition cannot be found. A complete breakdown of this issue and a proposed solution can be found in Berger et al. [54]

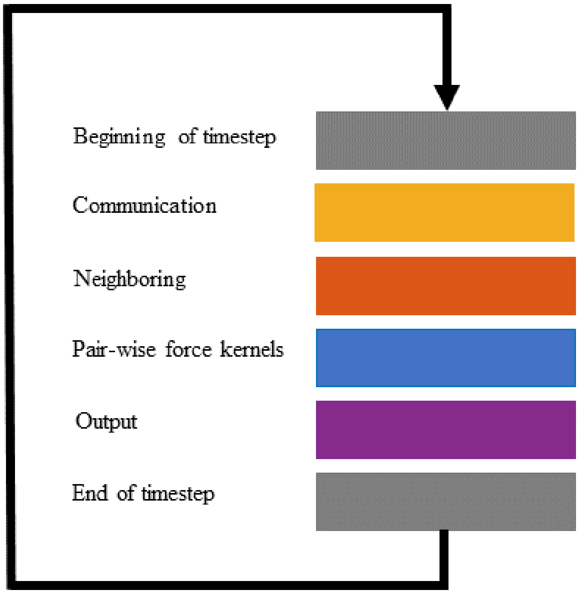

Figure 23 - Phases during a timestep.

Based on these premises, the use of the presented DEM model in a parallel environment required some tuning. The proposed domain decomposition consisted in slicing the computational domain along the direction of advancement of the recoater (x axis in Figure 18) with the extension of the slices varying throughout the simulation time. In order to verify the occurrence of any load imbalance due to the previously described phenomena a strong scalability test was performed. The test, along with the simulations that will be presented hereinafter, was performed on the LIGER supercomputer, a Tier2 BULLx DLC Parallel Scalar Supercomputer, running 266 bi-socket nodes Intel Xeon x86 E5-2680v3 2.5GHz 12 cores, with 14 nodes performing visualization optimization running on NVIDIA K80 cards and a high-speed interconnect network InfiniBand FDR (56 GBps) between nodes. The facilities are located in the campus of the École centrale de Nantes. The setup used for the strong scalability test is essentially the same as the one presented in section

3.3 but the dimension in the x direction is significantly increased in order to maintain the same ratio with the number of particles. Indeed, the simulation has a total of 320k particles and was run for 10k timesteps in the steady state. The same simulation was run doubling the number of processors each time up to a total of 64 processors. The results, in terms of total and single stage time are shown in Figure 24. A significant reduction in the total simulation time can be appreciated, confirming the validity of the proposed domain decomposition.

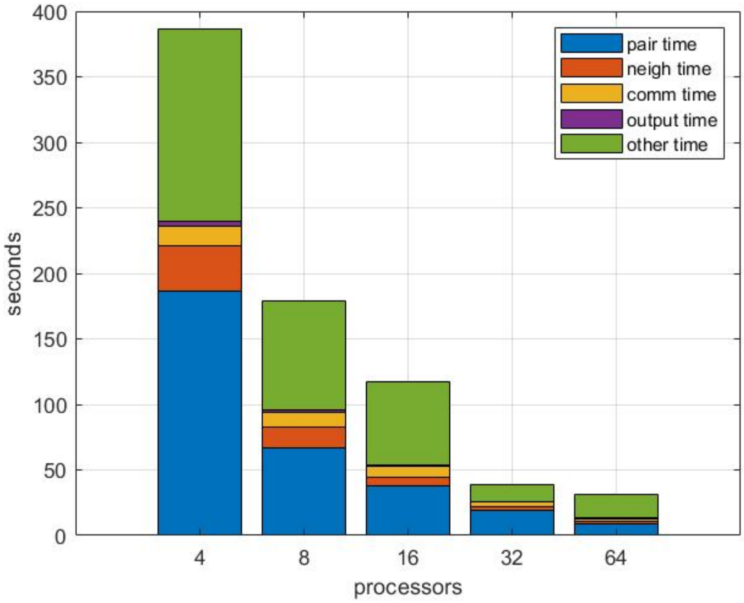

Figure 24 - Simulation time (total and phase wise) for 10k timesteps with 320k particles for different numbers of processors.

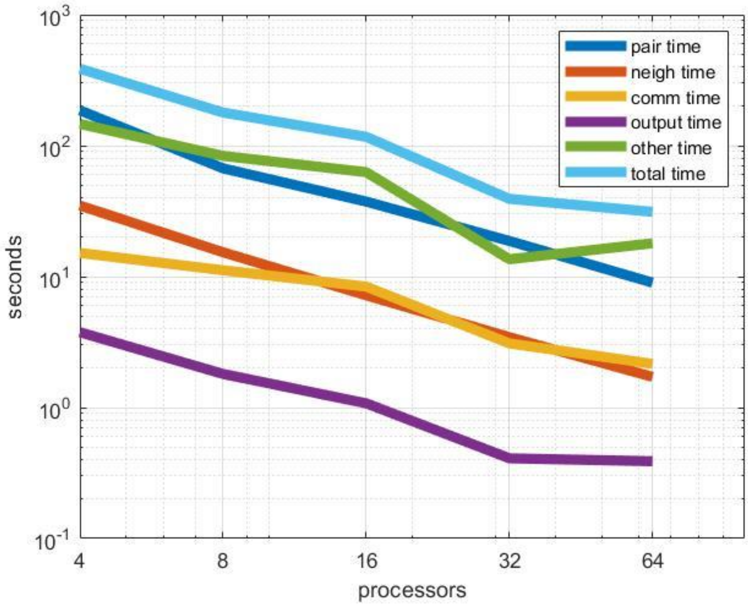

Figure 25 - Simulation time (phase wise) for 10k timesteps with 320k particles for different numbers of processors in double log scale.

Looking at the log-log plot in Figure 25 it can be seen that the speed up is almost linear up to 32 processors with an appreciable slowdown in the case of 64 processors. This result is not surprising considering that previous experiences, data on the code and test on the hardware have shown that even in ideal situations, the optimal number of particles per processors is around 10k, with rapidly degrading performances in case of more particles per processors. The speedup relative to the case of 4 processors is shown in Figure 26. The decrease is the efficiency with 64 processors is evident. The increased efficiency in the case of 32 processors is not surprising considering that the base reference is the time with 4 processors and stems from the previously discussed rule of the 10k particles for processors. Based on these results it can be concluded that the proposed model can be parallelized efficiently, making it possible to extend the computational domain without skyrocketing the time needed to perform the simulations. However, the scaling is not trivial. Indeed, in order to not alter the results, the ratio between the number of particles and the total length of the computational domain should be kept almost constant and since the minimum timestep to avoid numerical instabilities depends only on the characteristics of the particles (see section 3.3), taking into consideration more particles means expanding the computational domain and ultimately, due to the constant speed of the blade, more timesteps. Therefore, even if the parallelization negates an increase in wall time (i.e., he actual time that a program takes to run or to execute its assigned task) required per timesteps, the increase in the number of timesteps leads to longer simulations. Nonetheless, it is possible to complicate the simulations to faithfully reproduce the spreading process. Specifically, it is now possible to remove the two most limiting simplifying assumptions of the DEM model presented in this study: the single layer nature of the spreading process and the extension of the computational domain.

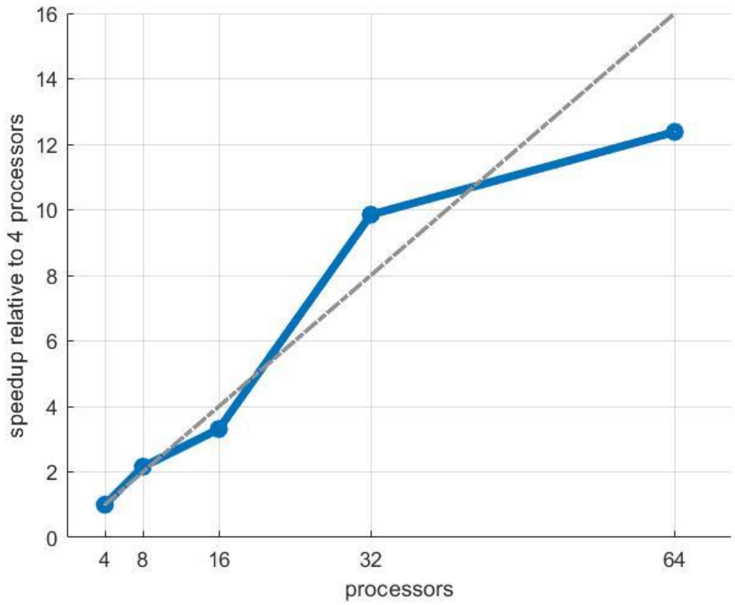

Figure 26 - speedup relative to 4 processors for 10k timesteps with 320k particles.

3.5 Multilayer

A real spreading process can be comprised of up to thousands of layers, therefore, a single layer simulation, while still providing useful insights, is bound to fail to fully capture the evolution of the phenomenon. Indeed, various studies in the literature have proven that the layer of spread powder can vary significantly during the process. Wischeropp et al. [55] developed an experimental setup to investigate the development of the actual powder layer height in successive layers, proving that there is a significant increase in the deposited powder, that can reach values up to 5 times the nominal layer thickness. Using a similar approach Jansen et al. [56] studied the effect of the process parameters on this increase, identifying a strong interdependence. In order to investigate these aspects, the DEM based model was slightly modified to take into account the recursive nature of the process. The total extent of the computational domain was increased to 10000 μm and the base mesh in the deposition zone (see Figure 18) can now move in the z direction effectively reproducing the lowering of the building plate in a 3D printer. After the first layer is spread new feedstock material is generated, the mesh is lowered by a distance equal to the nominally selected layer thickness and the spreading is repeated, with the previously spread layer now being the substrate. The process can then be repeated n times. To properly evaluate the results and to capture the effect of each layer on the subsequent ones also the characterization of the layer was improved to take into account the multi-layer nature of the process. Specifically, for each layer a series of inputs, identifying the conditions in which the spreading process takes place, and outputs, characterizing the results of the spreading process, were defined. The inputs, in the most general form, are the following:

- Nominal layer thickness (vertical shift of the deposition plate; **user defined**)
- Recoating speed (speed of the recoating device; **user defined**)
- Dose factor (total quantity of powder to be spread; **user defined)**
- Particle size distribution (PSD of the sample; **user defined**)
- Roughness (surface roughness of the previous layer; **model defined**)
- Void layer (space between the recoater and the free surface of the powder layer; **model defined**)

The inputs can be classified as either user or model defined. A user defined input can be set a priori while a model defined input results from the state of the previous layer and cannot therefore be controlled. The outputs, in the most general form, are:

- Effective layer thickness (position of the free surface of the powder bed)
- Real Effective layer thickness (thickness of the deposited layer of powders)
- Solid Volume Fraction Theoretical (solid volume fraction of the deposited layer of powders compared with an ideal full layer of nominal thickness)
- Solid Volume Fraction Real (solid volume fraction of the deposited layer of powders compared with an ideal full layer of real thickness)
- Particle Size Distribution (particle size distribution of the deposited layer)
- Roughness (roughness of the deposited layer)

Notice that, differently from the single layer case, the effective layer thickness does not give an exact representation of the depth of the newly deposited layer of powders. Indeed, the shape of the underlying substrate must be taken into account and therefore, a new parameter, the Real Effective Layer Thickness is introduced. The scheme in Figure 27 illustrates how some of the output for the layer n become input for the layer n+1. The output roughness of the layer n becomes straightforwardly the input roughness for layer n+1, while the void layer for the layer n+1 is a linear combination of other parameters and can be calculated as:

$$\mathrm{VL}(n+1) = \mathrm{NLT}(n+1) + \mathrm{NLT}(n) - \mathrm{ELT}(n) \quad (14)$$

Where VL is the void layer, NLT is the nominal layer thickness and ELT is the effective layer thickness.

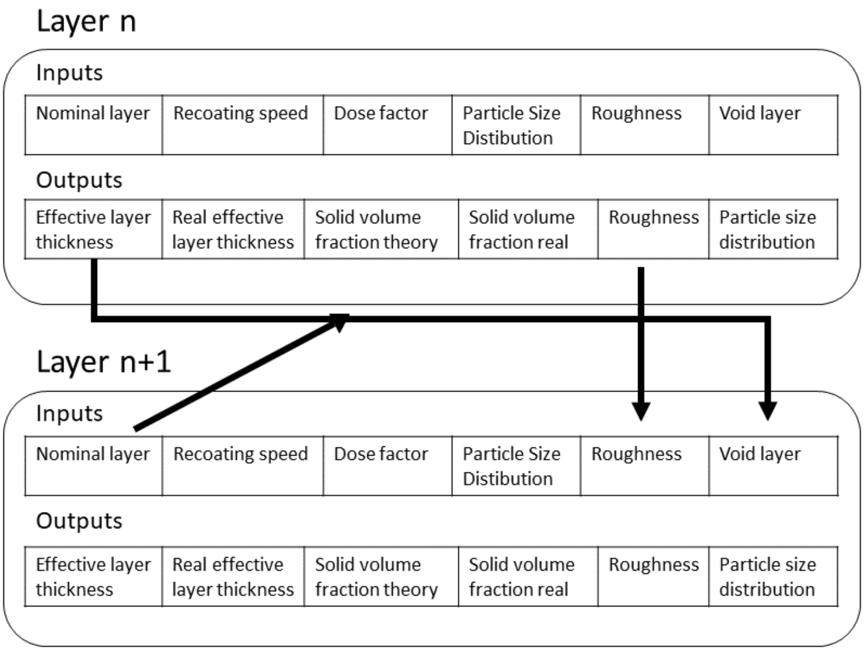

Figure 27 – Relationship between input and output of layer n and layer n+1

This improved model was used to perform multi layers simulations, in order to highlight the variation of the quantities of interest throughout the process. First, a monodisperse sample with a radius of 15 μm was considered, in order to reduce the number of variables. A total of 21 layers were deposited with a 50 μm nominal layer thickness and a 100 mm/s spreading speed. The results for the first 5 layers are presented in the figure from Figure 28 to Figure 32. It appears that the quantities of interest mean value varies significantly for the first layers, soon reaching a steady state. This phenomenon is enhanced by the monodispersed nature of the powders which promotes the formation of well-organized structures. Indeed, the solid volume fraction value is close the max theoretic value. For the first layer only two graphs are presented since the other two values are the same.

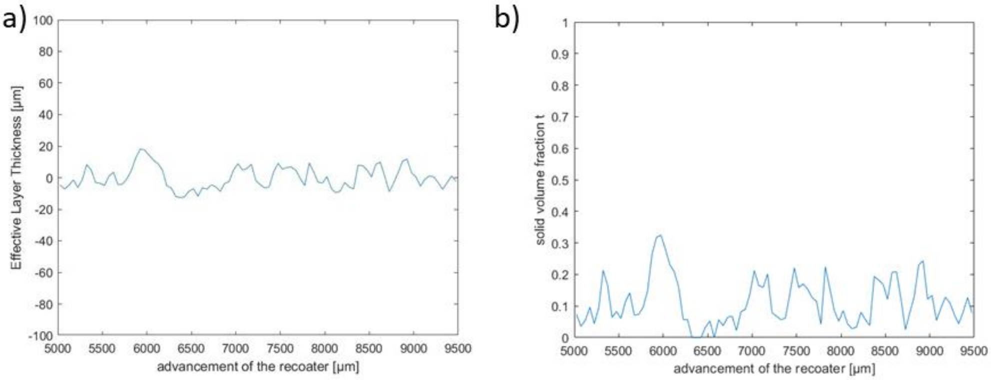

Figure 28 - a) Effective Layer Thickness and b) solid volume fraction theory for layer 1.

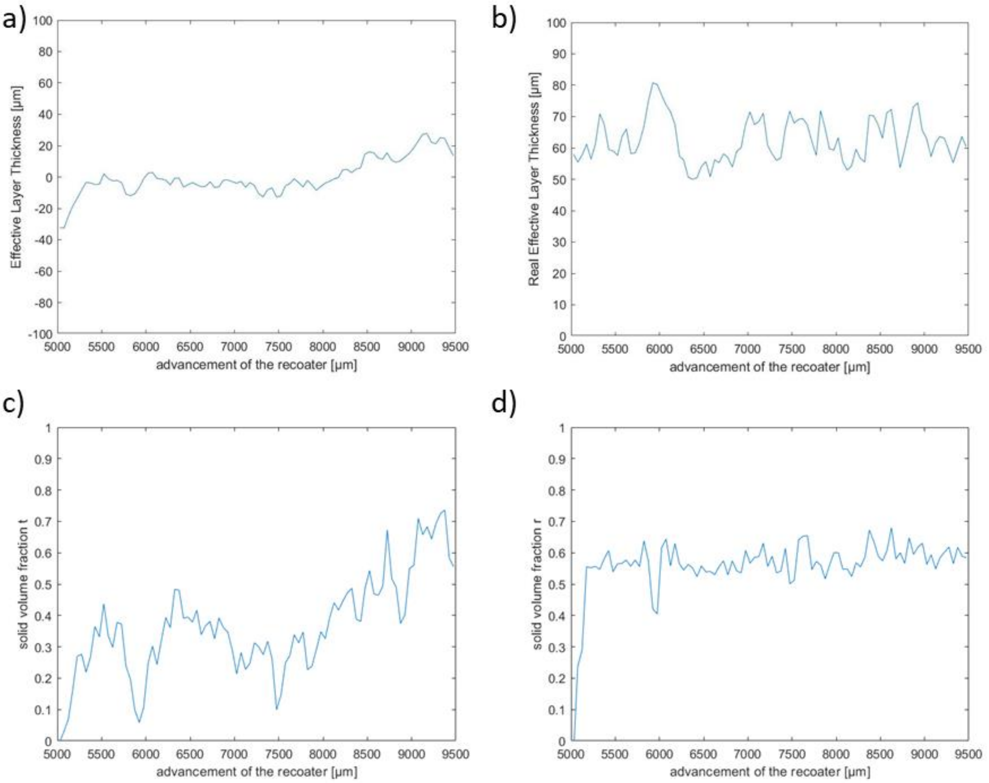

Figure 29 - a) Effective Layer Thickness, b) Real Effective Layer Thickness c) soldi volume fraction theory and d) solid volume fraction real for layer 2.

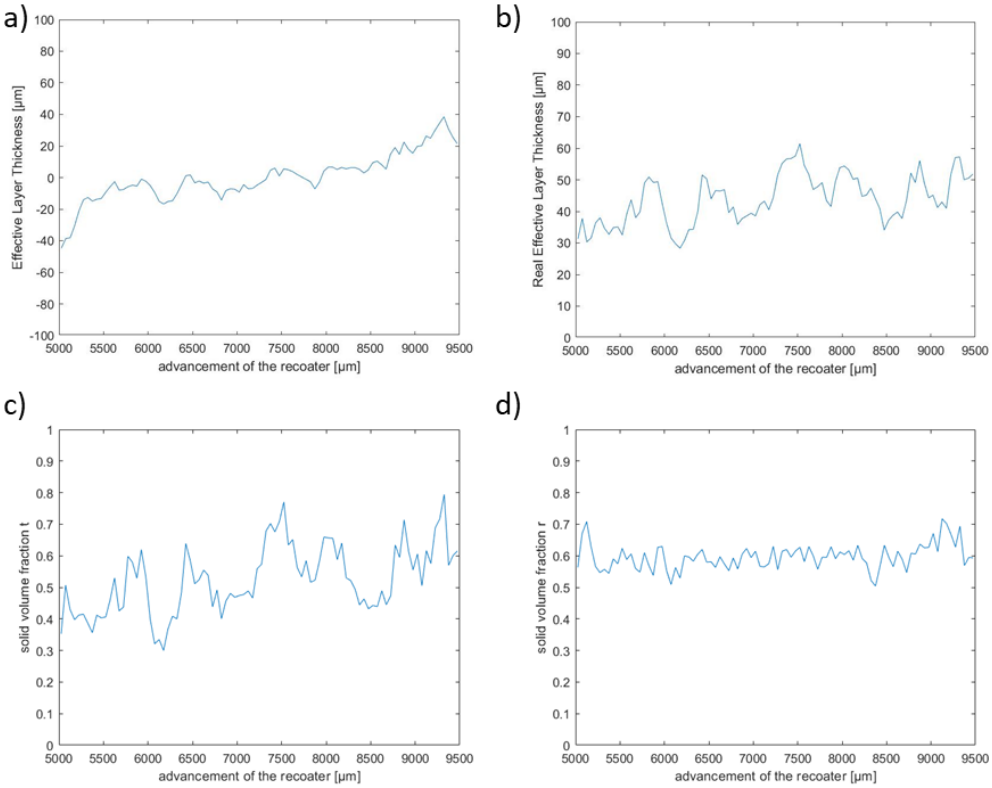

Figure 30 - a) Effective Layer Thickness, b) Real Effective Layer Thickness c) soldi volume fraction theory and d) solid volume fraction real for layer 3.

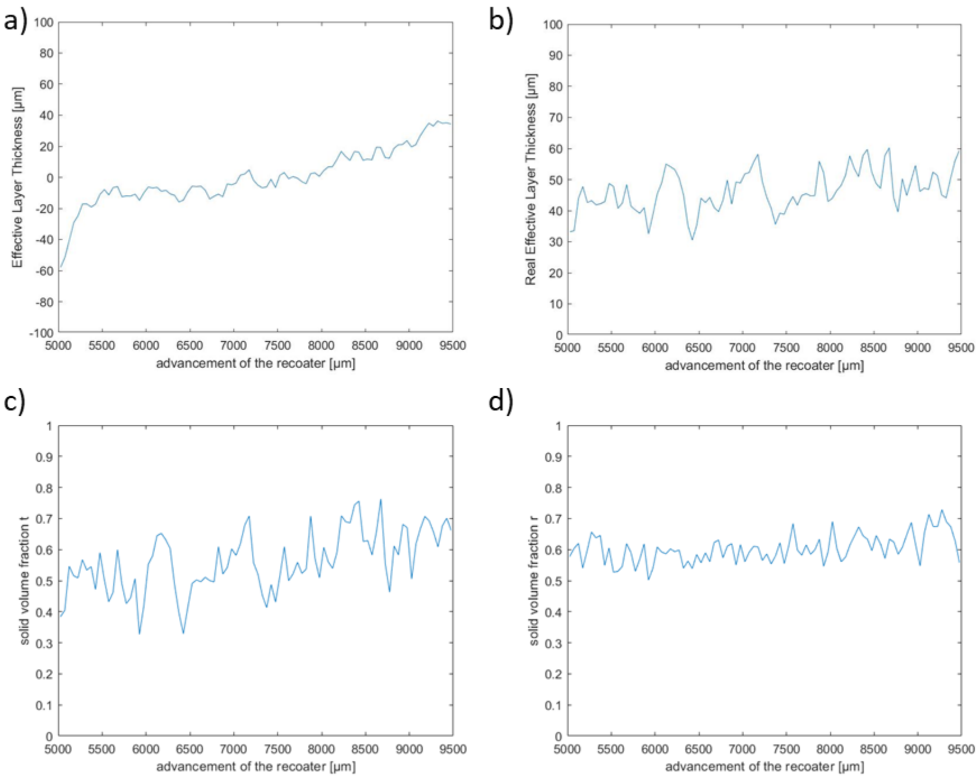

Figure 31 - a) Effective Layer Thickness, b) Real Effective Layer Thickness c) soldi volume fraction theory and d) solid volume fraction real for layer 4.

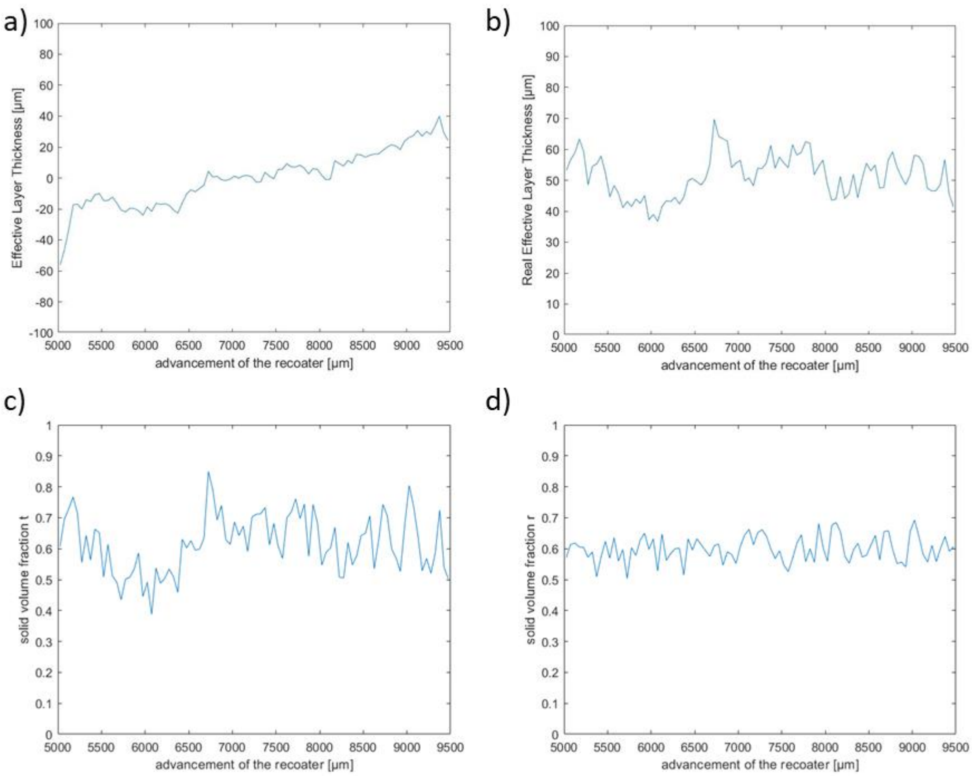

Figure 32 - a) Effective Layer Thickness, b) Real Effective Layer Thickness c) soldi volume fraction theory and d) solid volume fraction real for layer 5.

Looking at the graphs some of the findings of the single layer are confirmed. Specifically, the layer of deposited powders grows to a value bigger than the nominal layer thickness. Also, the slope of the powder bed can be found in each layer, with a hole in the initial zone and an accumulation of particles in the end of the computational domain. In this case the phenomenon appears more pronounced. No segregation was observed since all of the particles have the same radius. In order to verify the relation between the observed behaviour and the inputs the parameter space was explored, limited to the first three inputs reported in Figure 27 (i.e., nominal layer thickness, recoating speed, and excess powder) in a range that was deemed significant for potential application. The nominal layer thickness ranges from 30 to 70 µm, the recoating speed from 40 to 125 mm/s and the dose factor from 100 to 150% (100% meaning that quantity of powder to be spread is in theory equal to the powder to be deposited). To guarantee good representation of the real variability, a Latin hypercube sampling algorithm was used, and the resulting combinations are presented in Table 6.

Table 6 - Combination of input parameters resulting from the LHS.

Combination number	**Nominal layer thickness [µm]**	**Recoating speed [mm/s]**	**Dose factor [%]**
1	69	87	132
2	54	68	109
3	44	112	137
4	37	60	111
5	38	99	104
6	30	51	149
7	48	78	143
8	54	96	118
9	65	123	128
10	60	40	122

Multi-layer spreading simulations with these parameters were carried out. A total of 6 layer per combination was spread. Figure 33 trough Figure 42 show the evolution of the real effective layer thickness with every successive layer. Note that the plotted values refer to the average for the layer. It appears that the value of the real effective layer thickness increases rapidly in the first few layers to reach the value of the nominal layer thickness. The number of layers required for this stabilization decreases significantly for lower recoating speed. The dose factor does not have an evident effect.

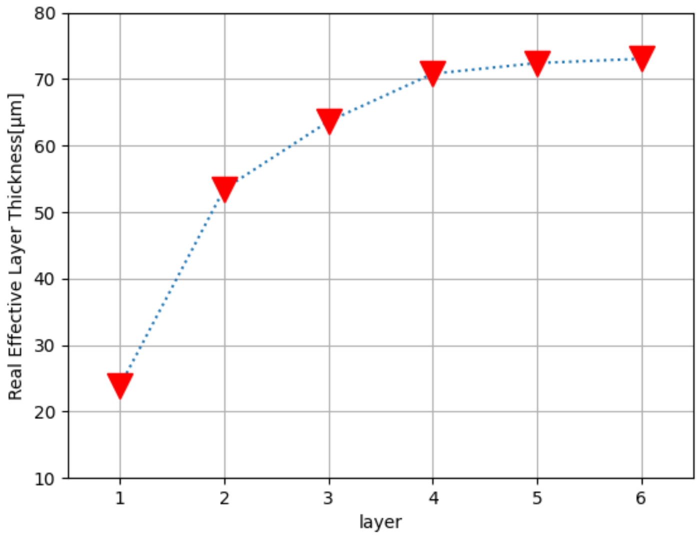

Figure 33 - Value of the real effective layer thickness as a function of layers for the combination of parameters number 1 in table 6.

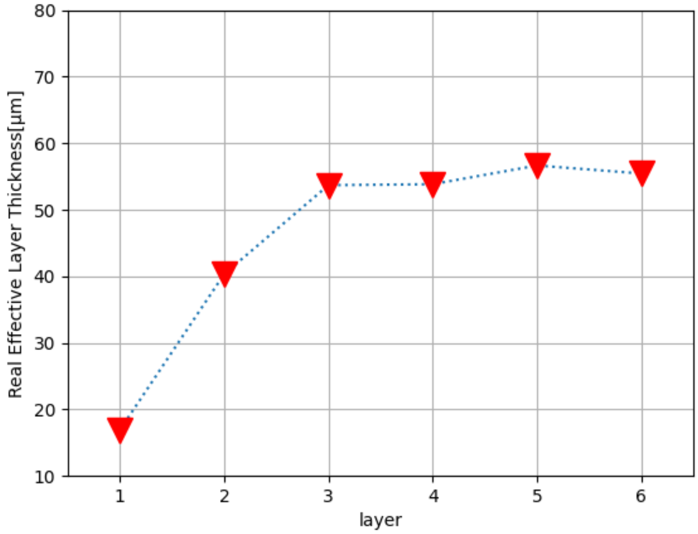

Figure 34 - Value of the real effective layer thickness as a function of layers for the combination of parameters number 2 in table 6.

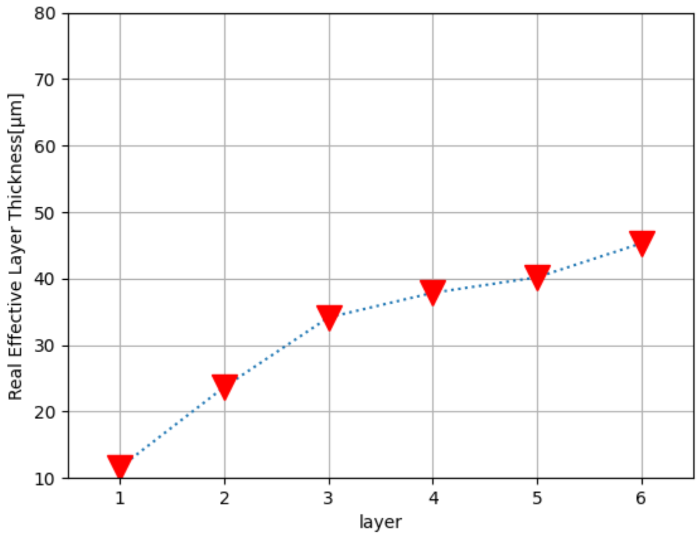

Figure 35 - Value of the real effective layer thickness as a function of layers for the combination of parameters number 3 in table 6.

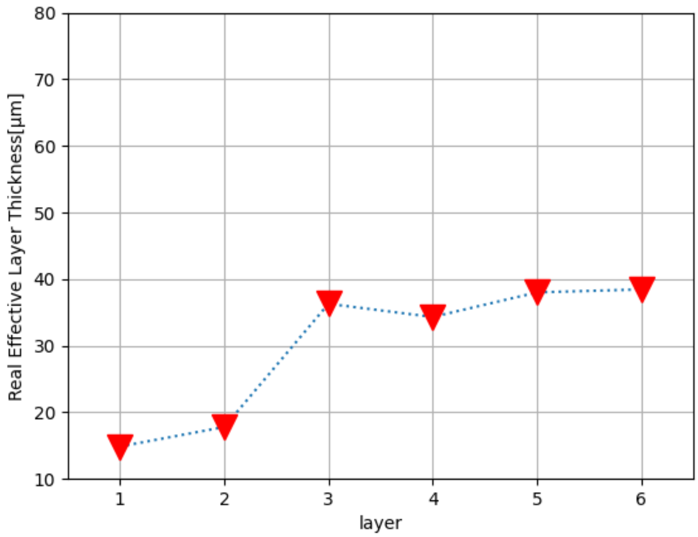

Figure 36 - Value of the real effective layer thickness as a function of layers for the combination of parameters number 4 in table 6.

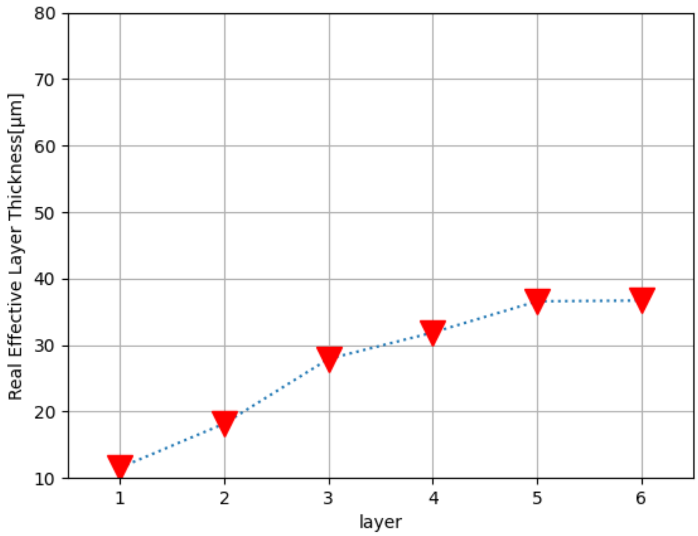

Figure 37 - Value of the real effective layer thickness as a function of layers for the combination of parameters number 5 in table 6.

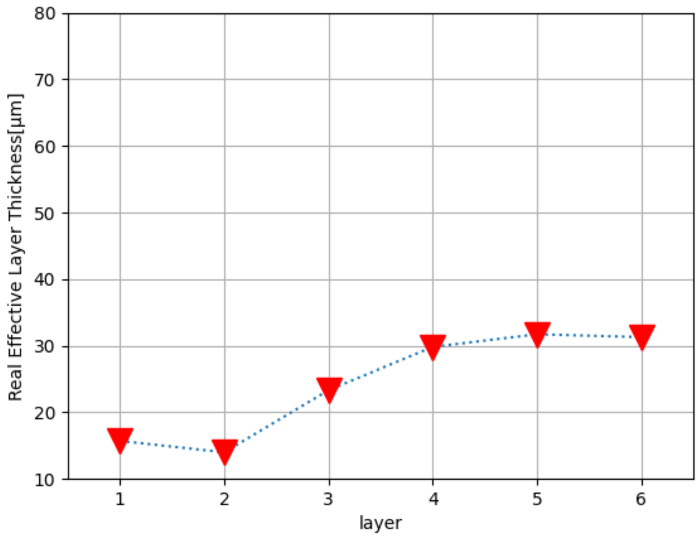

Figure 38 - Value of the real effective layer thickness as a function of layers for the combination of parameters number 6 in table 6.

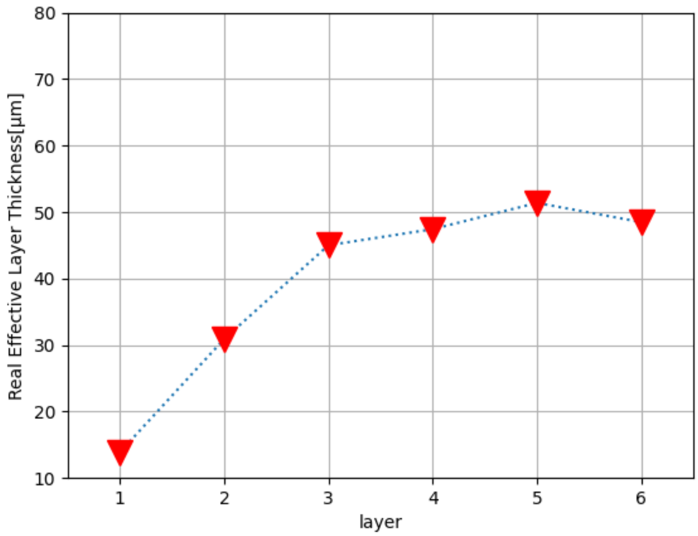

Figure 39 - Value of the real effective layer thickness as a function of layers for the combination of parameters number 7 in table 6.

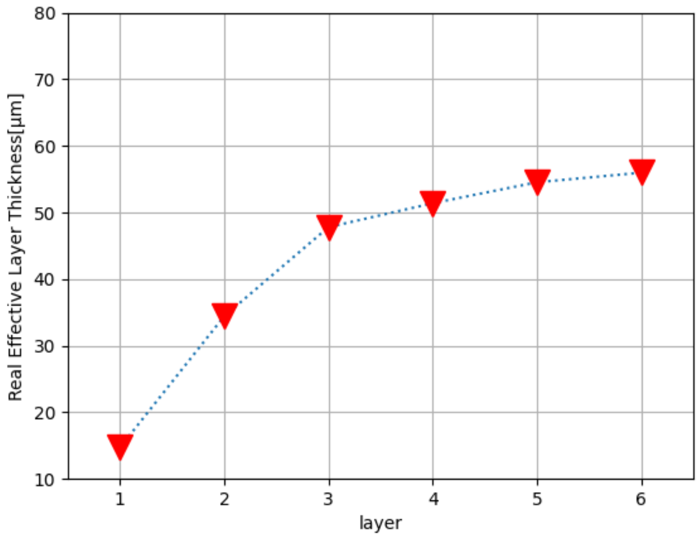

Figure 40 - Value of the real effective layer thickness as a function of layers for the combination of parameters number 8 in table 6.

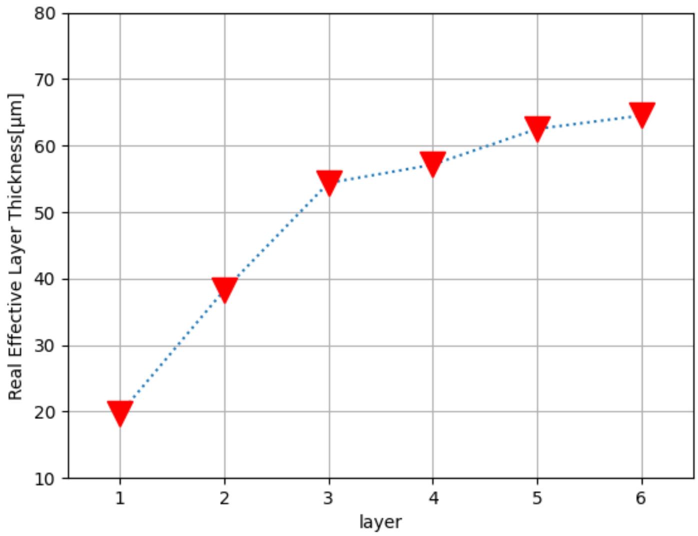

Figure 41 - Value of the real effective layer thickness as a function of layers for the combination of parameters number 9 in table 6.

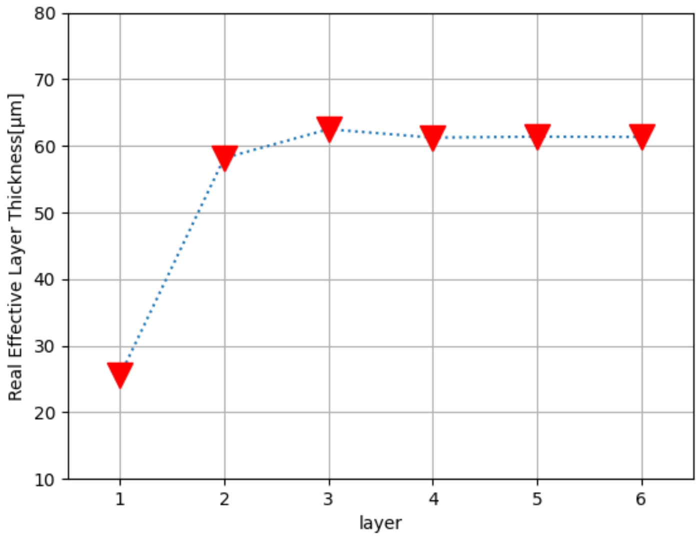

Figure 42 - Value of the real effective layer thickness as a function of layers for the combination of parameters number 10 in table 6.

3.5 Influence of a solid part

All of the multi-layer simulation presented until now are referred to free flowing layers of powder. That is, however, not always the case, for a LPBF process. Indeed, part of the powder bed is bound to be affected by the laser processing that melts the powders and leads to the formation of a solid part that is the goal of the printing process. This leads inevitably to modification in the spreading, with the new layer of powders now being spread on a layer that is a mix of free, unconstrained particles and a solid object, with his own geometric characteristic (i.e., roughness, shape, geometric singularity etc.), that can differ significantly from that of the spread layer of powders due to the complex phenomena that occur during the melting and solidification [57]. Also, given the arbitrary geometric complexity of the parts, complex combinations of free powder and solid parts can be encountered during the spreading process. In order to take into account these more complex configuration and to understand how they can affect the spreading process a new complication was introduced into our model. Part of each layer was transformed into a solid substrate, maintaining the surface properties. This process consists of two steps: first the surface of the particles in the zone of interest is reconstructed with a cloud of points, then a binning algorithm is applied to the point cloud and the point with max z is identified in each bin. These points are used to construct a mesh which acts as a substrate for the successive layer. Figure 43 summarizes the procedure and shows a typical result. The choice of the bin determines how much the feature of the underlying layer of powder are smoothed.

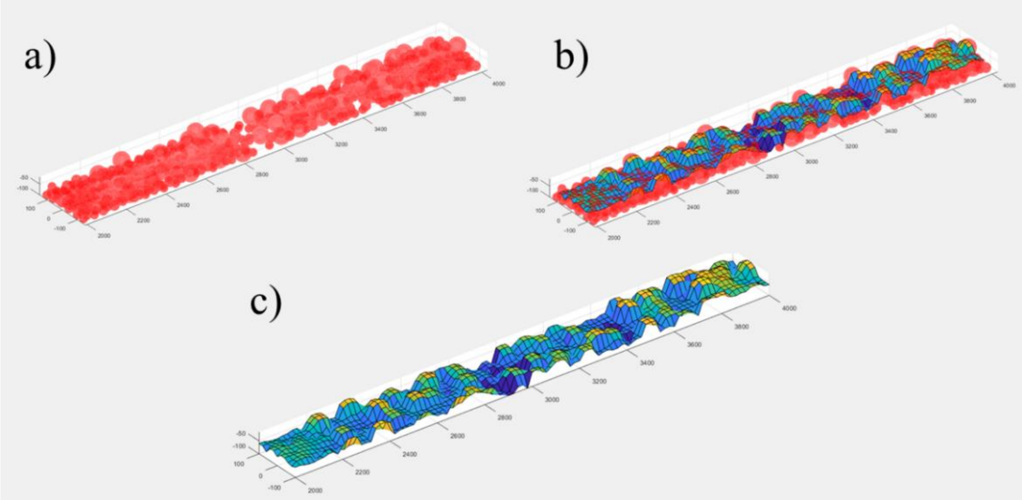

Figure 43 - Procedure used to mesh the layer: a) generation of the point cloud, b) binning and finding the max point per bin, c) reconstruction of the mesh.

While it should be clear that the substrate obtained with this procedure is far from representative of the state of the molten track of metal in case of a LPBF process (slightly closer to reality in case of simple sintering of the base powder) it still introduces a way of preserving the surface characteristics throughout the layers and taking into account the presence of a solid object in the powder layer. A new multi-layer simulation was performed introducing a meshed zone in the middle of powder bed (specifically the meshed zone extends from 6000 to 8500 μm). Similar to the free- flowing case, the quantity of interest (i.e., effective layer thickness, real effective layer thickness) changed significantly in the first few layers only to soon come to a stable value. The solid volume fraction showed a more interesting behaviour, as shown in Figure 44 trough Figure 47 (Notice that the graph for the first layer has been omitted since it is the same as the free-flowing case). Indeed, it can be observed that the solid volume fraction is significantly lower in correspondence of the meshed zone. The presence of a solid rough substrate disrupts the otherwise orderly structure that was observed in the free-flowing configuration. Moreover, voids can be observed at the beginning and at the end of solid zone. This “border effect” was also observed in the single layer simulations at the end of deposition zone, further confirming the disturbances caused by the presence of a solid part in the powder bed.

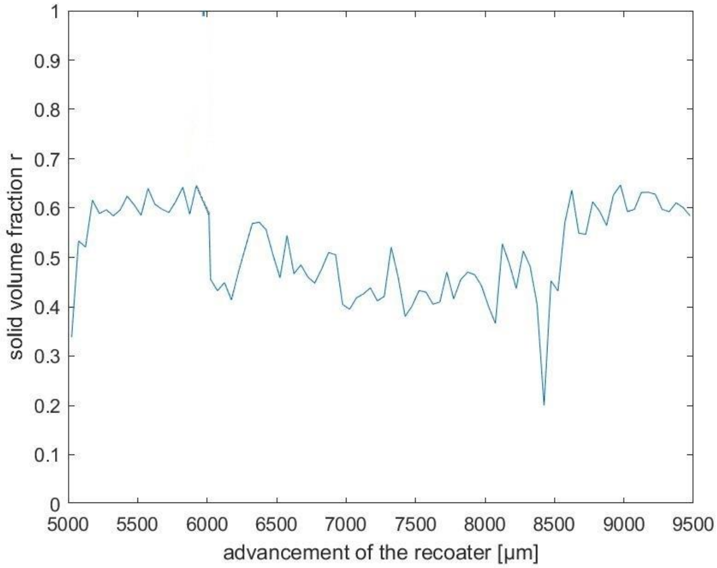

Figure 44 - Solid volume fraction real with meshed substrate for layer number 2.

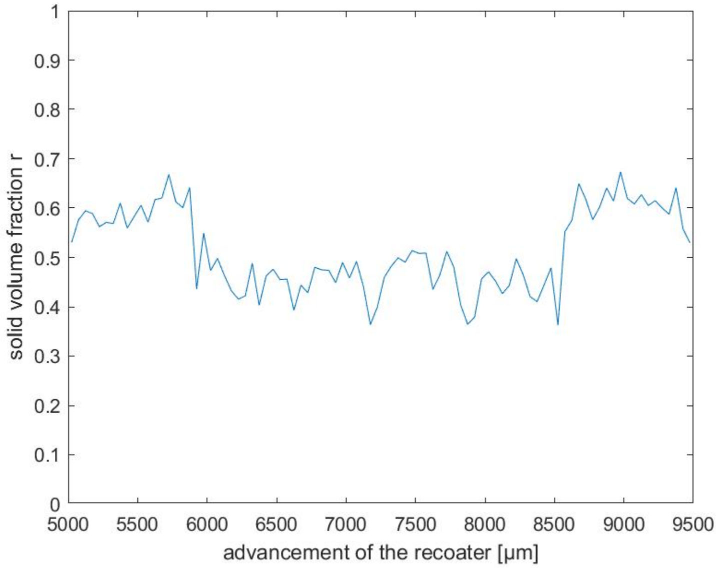

Figure 45 - Solid volume fraction real with meshed substrate for layer number 3.

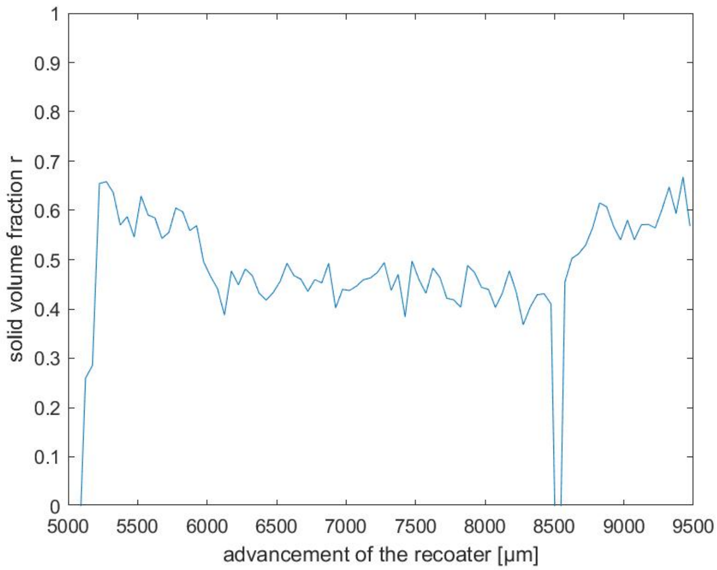

Figure 46 - Solid volume fraction real with meshed substrate for layer number 4.

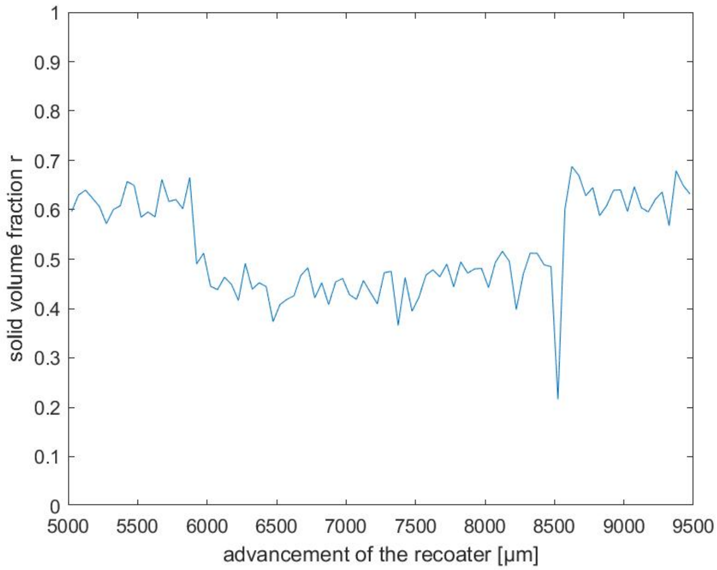

Figure 47 - Solid volume fraction real with meshed substrate for layer number 5.

The presented DEM based model provided useful insights on the phenomena that take place during the spreading process and how to optimize it to obtain the desired powder bed characteristics. It showed good scalability and proved to be able to capture the time evolution of the process throughout the spreading of successive layers. A practical application of the model and how, at his actual stage, it can be used to improve the results of a 3D printing process. Nonetheless, some upgrades are needed to obtain a more faithful description of the process. Specifically, a model for the layer processing stage (widely available in the literature) should be integrated into the loop for the multi-layer simulation.

Section 4: Application

4.1 Motivation

This section will present a case study, highlighting the importance of a clearer comprehension and optimization of the spreading process. The information and techniques presented in this work will be applied to the 3D printing of a custom alloy, aiming at improving the energy efficiency of the process, showcasing how an optimized spreading process can have a significant impact on an industrial setting. Indeed, the possibility to produce parts with customized mechanical properties, acting directly on the provided feedstock material. Aluminium alloys have received great interest as they are the main materials in aerospace industries due to their low density and high strength combined with good processability and mechanical properties. Among these, one of the most studied is the AlSi10Mg due to its good mechanical properties coupled with a relatively good printability [58]. It has been proven that the properties of this alloy can be further enhanced by adding between 2% and 6% of Cu [7]. Indeed, the printing of a mixture of Al based alloys with the addition of a small percentage of Cu has been attempted successfully from various authors. Namely, Zhang et al. [59] fabricated crack-free Al-Cu-Mg parts, finding that the laser energy density value of 340 J/mm^3 is the threshold above which samples without imperfections can be obtained. Nie et al. [6] examined the impact of the scanning speed on single tracks and the overlapping effect on multitrack parts of Al-Cu-Mg alloys, reaching optimal results for an energy density ranging from 150 to 170 J/mm^3. Della Gatta et al. [7]successfully produced Al-Si-Mg-Cu parts by mixing AlSi10Mg and pure Cu powders, investigating the process window 35–180 J/mm^3. Much more studies are available for the SLM of AlSi10Mg without any copper addition, but the energy densities adopted are roughly in the same range [60]–[64]. It can be noted that the energy density required to obtain an effective process is generally higher than 100 J/mm^3. This is associated with the high reflectivity and high thermal conductivity of aluminium compared to other alloys. Indeed, 3D printing of materials with higher melting temperatures, such as Inconel, Steel, or Titanium, are smaller. For example, the energy densities required for the SLM are 56–80 J/mm^3 for stainless steel, 37–85 J/mm^3 for IN718-Cu, and 40–70 J/mm^3 for Ti6Al4V. These observations suggest that the heat transfer from the laser to the powder plays a pivotal role in the printing of the samples. Indeed, the relation between the input energy and the processed material is not straightforward and it is regulated by the complex laser-matter interaction. the reason for this apparent contradiction lies in the state of the underlying material to be processed which is rarely taken into account [9], [65]. The key idea is to investigate the possibility of reducing the energy required to achieve an effective printing for an Al- Si-Mg-Cu alloy by enhancing the “energy absorption efficiency” defined as the ratio between the energy absorbed by the powder bed and the one provided by the laser beam. This will be carried out in a two-step process. In the first stage, the DEM based model presented in the previous section will be used to evaluate the optimal value for layer thickness and spreading speed to maximize the packing factor and the surface coverage. Then, in the second step, several specimens are printed with the parameters determined by the model and the results are evaluated based on the relative density, the porosity, and the microhardness.

4.2 Materials and methods

4.2.1 Feedstock material

The numerical model used in this case study is based on the on presented in detail in the previous section, however some modifications are mandatory. First, the material used in this case is different: AlSi10Mg and 99% pure Cu gas atomized powders with Figure 48 showing SEM images of both powders.

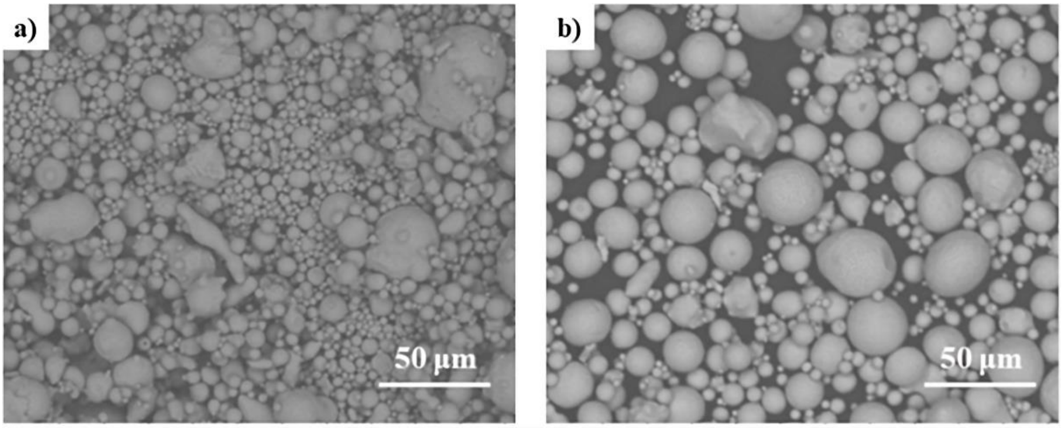

Figure 48 - SEM images of the powders used as base materials: (a) AlSi10Mg; (b) Cu.

The chemical composition of the AlSi10Mg powder, as declared by the supplier, is reported in Table 7.

Table 7 - Chemical composition of AlSi10Mg powder.

Al	Si	Mg	Fe	Mn	O	Ti	Cu	Zn	C	Ni	Pb	Sn
Bal.	9.0–11.0	0.20–0.45	0.55	0.45	0.20	0.15	0.10	0.10	0.05	0.05	0.05	0.05

The powders are mixed with weight ratio of 4% Cu and 96% using a fluidized bed facility operating with Argon, supported by an acoustic field to avoid aggregation between the different clusters of particles. The effectiveness of the mixing process is verified through SEM images of the mix (Figure 49) where the Cu particles are indicated by a lighter colour.

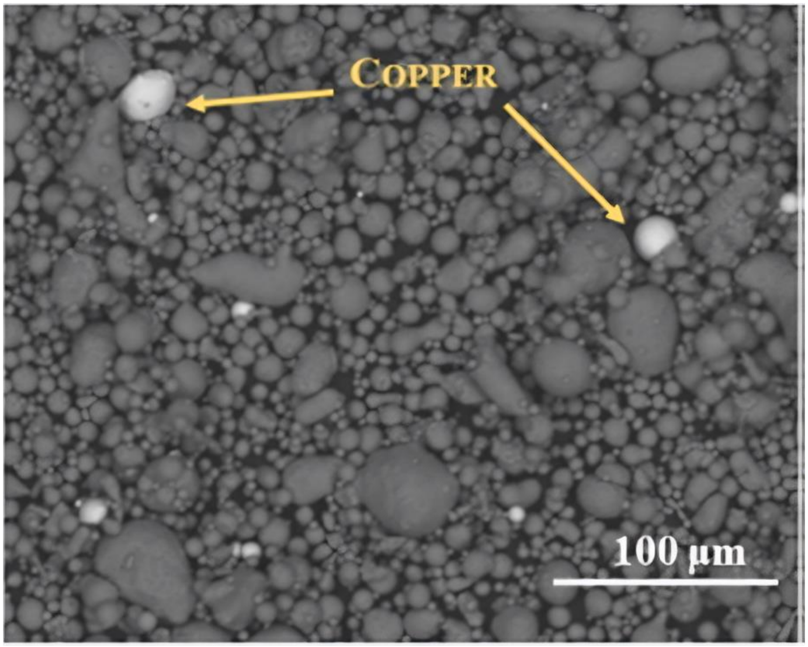

Figure 49 - SEM image of the mixed powder used as feedstock material. The Cu particles are indicated by a lighter color.

The material properties have been varied to reflect these changes, using the procedures explained previously. The same applies to values for the spreading parameters optimization.

4.2.2 Optimization of the spreading process

Two values of the layer thickness are considered, 30 μm and 50 μm, typically used in SLM industrial applications for the considered material [27]. Regarding the spreading speed, since high values have proven not suitable the choice fell on values in a lower range. Specifically, 75, 50, and 25 mm/s, for a total of 6 different combinations. Figure 50 and Figure 51 show a comparison of the powder bed for the three different values of the spreading speed and a layer thickness of 50 μm and 30 μm, respectively.

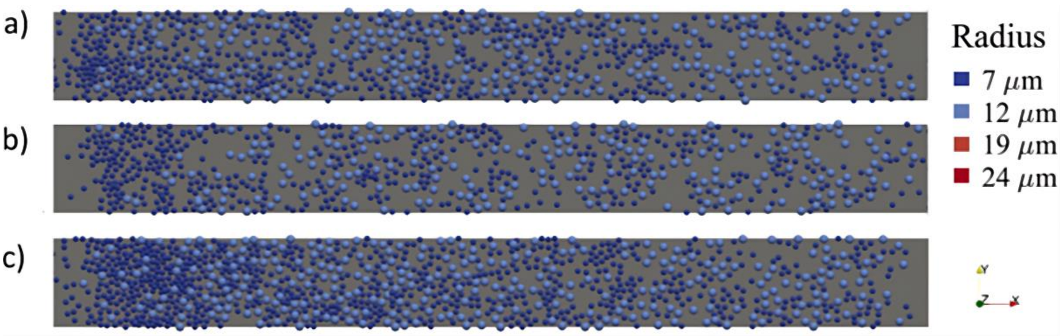

Figure 50 - Results of the simulations with a 30 μm layer thickness for different levels of spreading speeds: (a) 75 mm/s, (b) 50 mm/s, and (c) 25 mm/s.

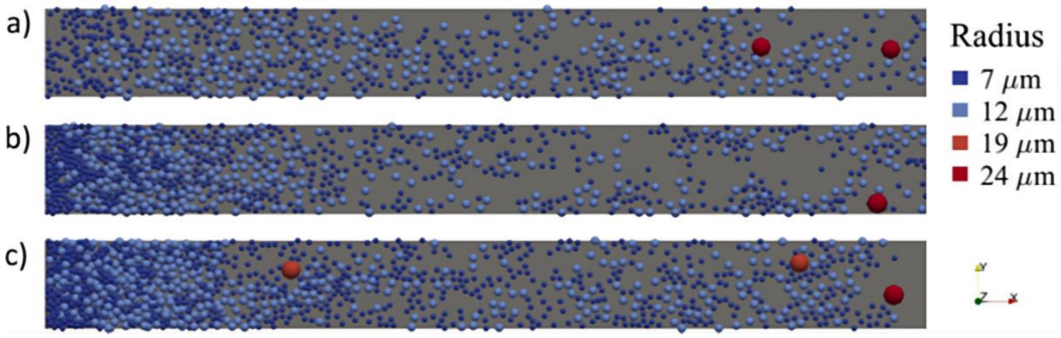

Figure 51 - Results of the simulations with a 50 μm layer thickness for different levels of spreading speed: (a) 75 mm/s, (b) 50 mm/s, and (c) 25 mm/s.

A first result that can be observed is the substantial modification of the size distribution of the deposited particles between the two configurations. Indeed, for a layer thickness of 30 μm the biggest particles are almost absent since the gap between the layer and the solid substrate acts as a filter, effectively dragging them away. These particles are caught in the powder heap in front of the blade and are not deposited in the powder bed with a phenomenon similar to that observed and discussed in the previous section. This also determines a significant deterioration of the characteristics of the powder bed (i.e., surface coverage and solid volume fraction) along the spreading direction. The surface coverage is obtained as the fraction of the area of the layer that is covered by the particles. A low value of this parameter means that there are holes in the powder bed where no particles have been deposited. As for the solid volume fraction, it is calculated as the total volume occupied by the particles, divided by the theoretical volume of the layer (a parallelepiped with a height of 30 μm or 50 μm, depending on the layer thickness). The results are plotted in Figure 52 and Figure 53. The surface coverage decreases significantly with increasing the spreading speed and appears to be rather insensitive to the layer thickness variation. Similarly, the solid volume fraction decreases with increasing the spreading speed; however, the impact of the layer thickness is more relevant, with a thicker layer resulting beneficial for a more compact powder bed. The above results suggest that the optimal parameters to be used in the experiments are a layer thickness of 50 μm and a spreading speed of 25 mm/s. However, in the experimental tests, the speed of the recoating device is set to 35 mm/s, a slightly higher value to reduce the processing time.

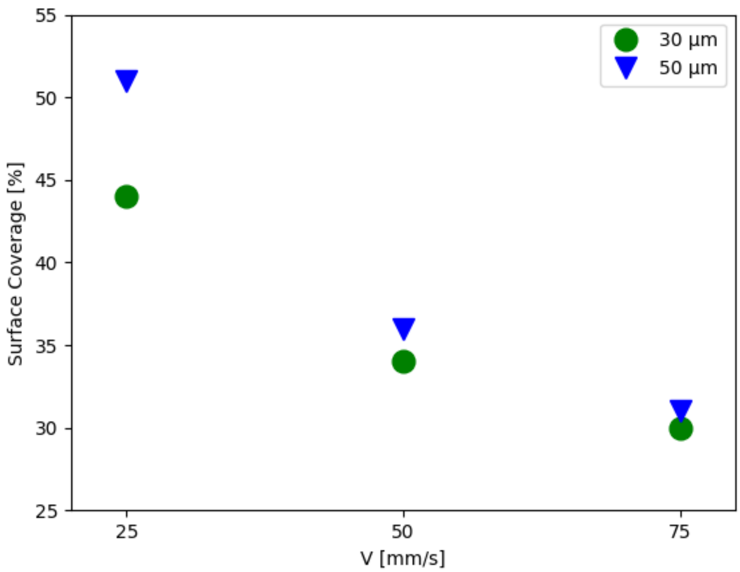

Figure 52 - Surface coverage for different spreading velocities and layer thicknesses.

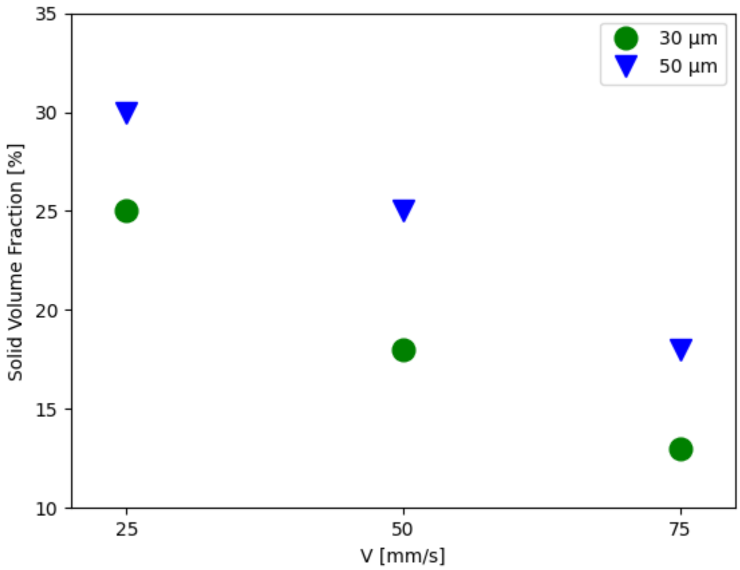

Figure 53 - Solid volume fraction for different spreading velocities and layer thicknesses.

The SLM process is performed by using a Concept Laser M2 Machine operating in Argon atmosphere. As anticipated the whole purpose of this case study was to obtain a satisfactory printing with a reduced energy density. Therefore, three different levels of energy densities (20, 25, and 35 J/mm^3) are investigated. Moreover, the energy effectively adsorbed by the material may vary depending on the adopted values of laser power and scan velocity The processing parameters are related by the following formula:

$$E_d = \frac{P}{V_s h_s L_t} \tag{15}$$

Where E_d is the energy density, P is the laser power, V_s is scan velocity, h_s is the hatch spacing, and L_t is the layer thickness. The hatch spacing, i.e., the separation distance between two consecutive laser beams (orthogonal to the laser scan direction), is kept constant at 0.09 mm. A complete overview of the different processing condition is reported in Table 8.

Table 8 - Experimental processing conditions.

Set of parameters	**P[W]**	**Vs[mm/s]**	**h[mm]**	**Lt[mm]**	**Ed[J/mm^3]**
1	150	952	0.09	0.05	35
2	180	1143	0.09	0.05	35
3	210	1333	0.09	0.05	35
4	240	1524	0.09	0.05	35
5	150	1111	0.09	0.05	30
6	180	1333	0.09	0.05	30
7	210	1556	0.09	0.05	30
8	240	1778	0.09	0.05	30
9	150	1333	0.09	0.05	25
10	180	1600	0.09	0.05	25
11	210	1867	0.09	0.05	25
12	240	2133	0.09	0.05	25

4.2.3 Printed samples characterization

For each processing condition, three samples (10x10x10 mm^3) are printed, randomly positioned across the building plate to avoid the influence of the building position on the measured properties. The surface roughness of the top face of the as-built cubic samples is examined with a Confocal Microscope (Leica DCM3D Scan) [66]. The surface roughness parameters considered in this study are the arithmetic mean surface roughness and the maximum height according to the standard ISO 25178-2. The sample density ρ_s is evaluated according to the Archimedes method by using a Gibertini Infinity balance and calculated as:

$$\rho_s = (\rho_{water} - \rho_{air}) \frac{m_{air}}{m_{air} - m_{water}} + \rho_{air} \tag{16}$$

With ρ_{water} and ρ_{air} the densities of water and air at 25 °C, and m_{water} and m_{air} the weights of the sample in air and water, respectively. Denoting with $w_{AlSi10Mg}$ and $\rho_{AlSi10Mg}$ the mass percentage and density of AlSi10Mg, and with w_{Cu} and ρ_{Cu} the mass percentage and density of Cu, the theoretical density of the alloy is calculated as:

$$\frac{1}{\rho_t} = \frac{w_{AlSi10Mg}}{\rho_{AlSi10Mg}} + \frac{w_{Cu}}{\rho_{Cu}} \tag{17}$$

The relative density (RD) is measured concerning the material theoretical bulk density of 2.72 g/cm^3 and then expressed as:

$$\mathrm{RD} = \frac{\rho_s}{\rho_t} \times 100 \tag{18}$$

The relative density measurements are repeated three times for each sample. For microstructural observations and microhardness measurements, the cubes are sectioned via a metallographic hacksaw to observe the cross-section containing the build-up direction. Then, the cut samples are hot mounted in epoxy resin, and subsequently mechanically grounded on sandpapers and then polished with diamond suspensions. Observations of the cross-sections of the samples are made with an optical microscope (Figure 54 panel a). To observe the microstructure, the surfaces of the mounted samples are etched with chemical reagent (Keller). The images are post processed via image analysis software, to enhance the contrast between voids and metal parts and to calculate the amount of porosity in the samples. To analyse the gradient of the porosity, each sample is divided in bottom, centre, and top part. A typical result is shown in Figure 54 panel b and c.

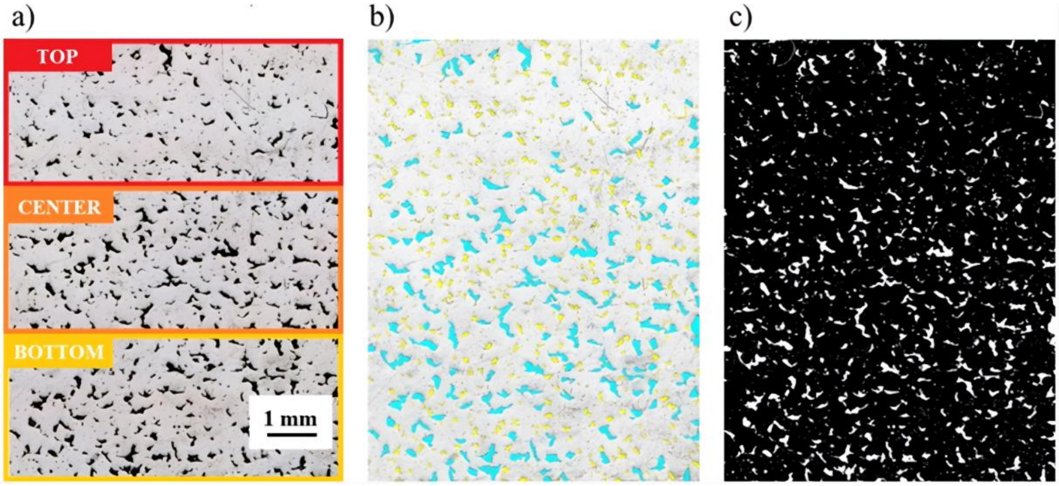

Figure 54 - Steps of image analysis: (a) optical acquisition of the cross-section, (b) identification of the porosities, (c) image mask.

To determine the mechanical properties, micro-hardness tests are performed. Hardness is measured according to the Vickers scale by using a Micro-Vickers Hardness Tester. The test is repeated nine times in various positions of the sample to ensure the repeatability of the measurements.

4.3 Results

4.3.1 Surface roughness

An overview of the results of the printing process for each processing condition is presented in Figure 55.

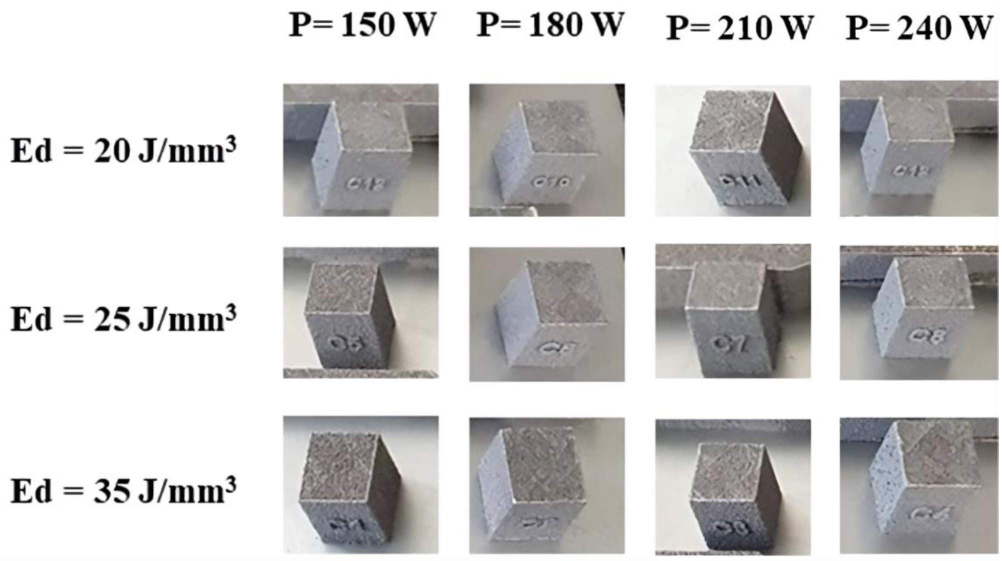

Figure 55 - Overview of the printed samples with the respective processing conditions.

A variety of flaws arise on the sample surfaces as a result of various phenomena that take place during the SLM process, making it challenging to evaluate the roughness and interpret the data. In order to accurately assess the quality of each scanned layer during the construction process, it is crucial to focus on the top surface's roughness. Figure 56 reports a sample of the acquired surface.

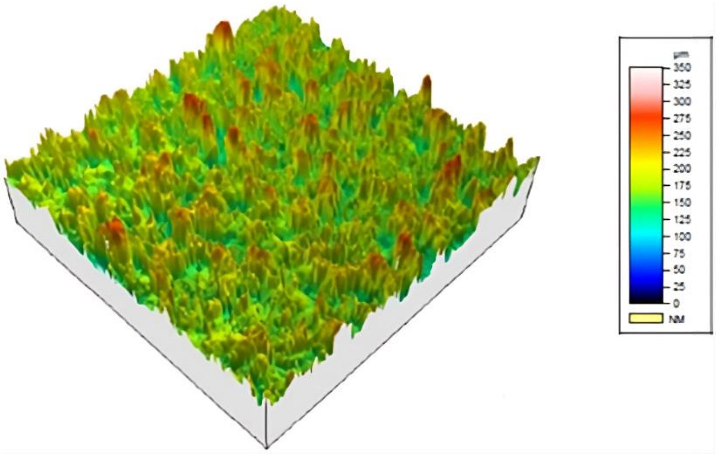

Figure 56 - Rendering of the acquired top surface of sample 1.

The samples' surfaces have several superficial clusters, which show that the powder hasn't completely melted in those areas. However, there are no external breaks or missing pieces in the samples. Figure 57 display the outcome of the roughness measurement for each sample. The average values vary from 20 to 34 µm, and values fall between 270 and 378 µm. When the process parameters are changed, neither surface morphology parameter generally exhibits an evident trend, which points to a complex phenomenology. However, the data show that the lowest values are reached at the highest laser power, indicating a smoothing effect brought on by the rise in power.

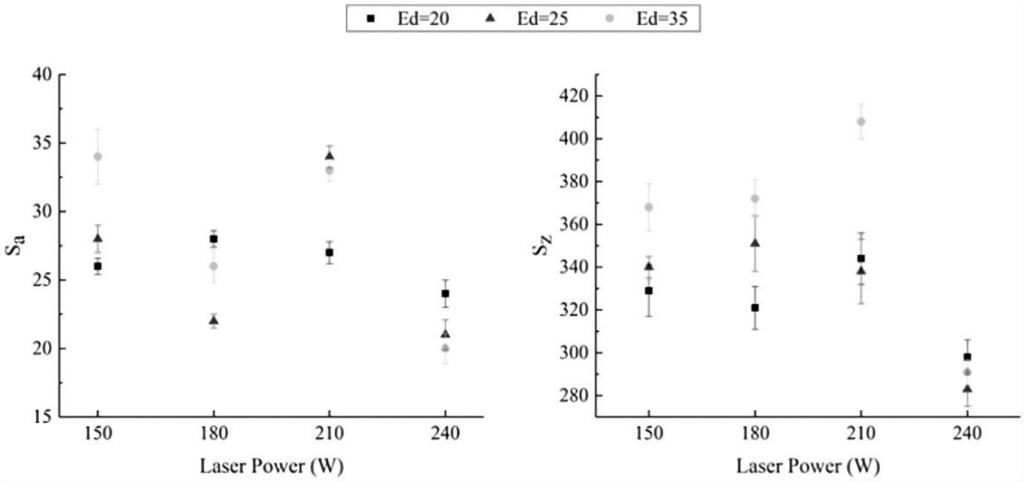

Figure 57 - Measured Sa (left) and Sz (right) compared to the process parameters.

4.3.2 Density

Other than the characteristics of the top surface it is pivotal to evaluate the densification and the presence of internal defects in the printed part. Indeed, the presence of a great number of porosities or other defects can compromise the integrity of a printed part and should therefore be avoided. In general, in a LPBF process, two types of processing defects can be identified that are related to the employed energy density in an opposite way: lack of fusion (LOF) and keyholes. LOF defects form when the energy is insufficient to obtain a full melting of the powders. Causes can be an excessively low laser power or a scan velocity too high. Keyholes, on the contrary, happen when, due to excessive energy density, a fluid dynamic instability forms in the molten pool [67]. The analysis of the quantity, size, and geometry of the defects indicates whether the process parameters are above or below the optimum values. In this light, for in-depth analysis of the internal defects in the specimens, the crosssectional morphologies parallel and perpendicular to the building direction are taken for metallographic observation. The dependence of the porosity and the relative density of the samples on the laser power and scanning velocity is investigated for different energy densities. In Figure 58 the measured relative density is plotted against the laser power.

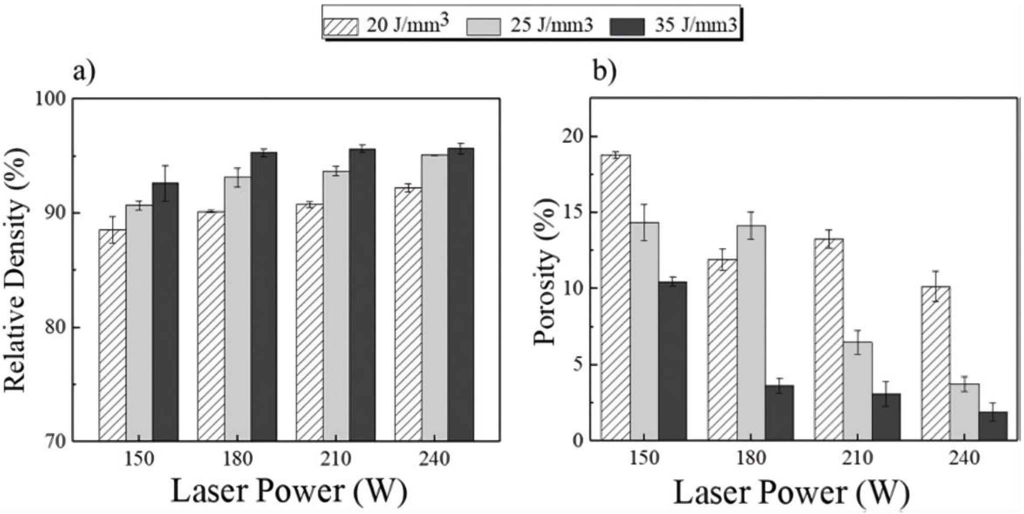

Figure 58 - (a) Relative density and (b) porosity measurements compared to the laser power and the energy density.

It can be noticed that the relative density increases by increasing the energy density, reaching a value of 96% for an energy density of 35 J/mm^3. Also, for each investigated value of energy density, the relative density increases for increasing values of the laser power and scanning velocity. Most samples reveal irregularly shaped pores and some un-melted powder particles can be identified. These defects can be attributed mainly to lack of fusion or rapid solidification of the metal without complete filling of gaps. From a visual analysis of Figure 59, a similar trend for each value is identified: numerous and large LOF defects exist in samples built using a laser power of 150 W, whereas they start to decrease in number and dimension when increasing the power up to 240 W, showing that, despite the optimization of the spreading process, a higher energy density is required to attain a complete melting and a stable process. Among the investigated processing conditions samples are printed at = 240 W and = 35 J/mm^3.

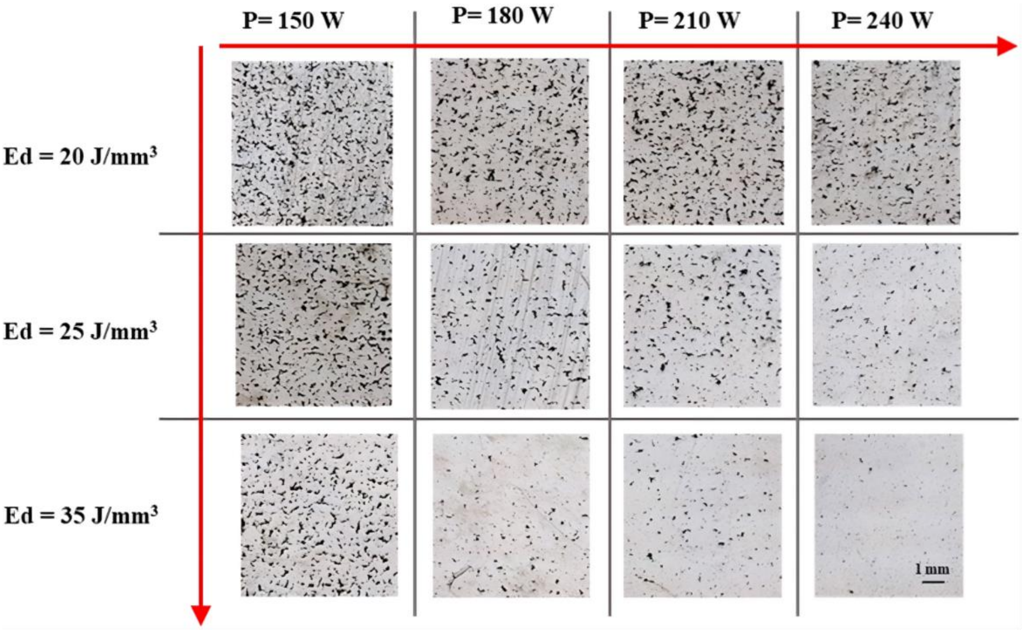

Figure 59 - Images of the cross-section of the samples with the respective processing conditions.

However, it can be interesting to focus on the variation of the defects in the same specimen throughout the printing process. As explained previously, the cross-section of the samples has been divided into three parts in order to analyse how the presence of porosity changes throughout the sample height.

For each set of parameters, the porosity slightly decreases from the bottom of the sample to the top. This behaviour is more evident when increasing the energy density and decreasing the laser power as shown in Figure 60 trough Figure 62.

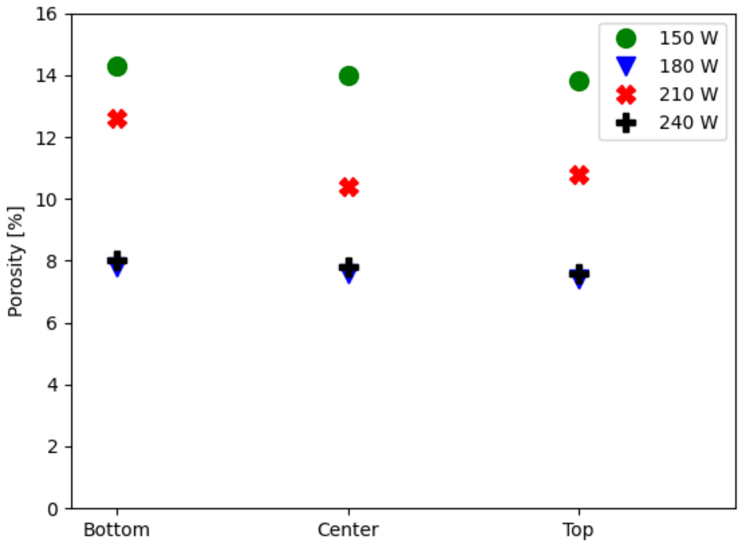

Figure 60 - Porosity variation through the specimen for E_d = 20 J/mm^3

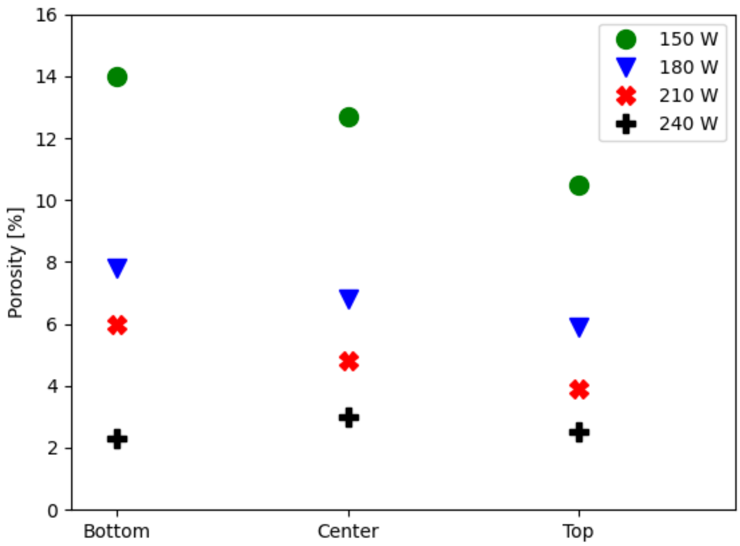

Figure 61 - Porosity variation through the specimen for E_d = 25 J/mm^3

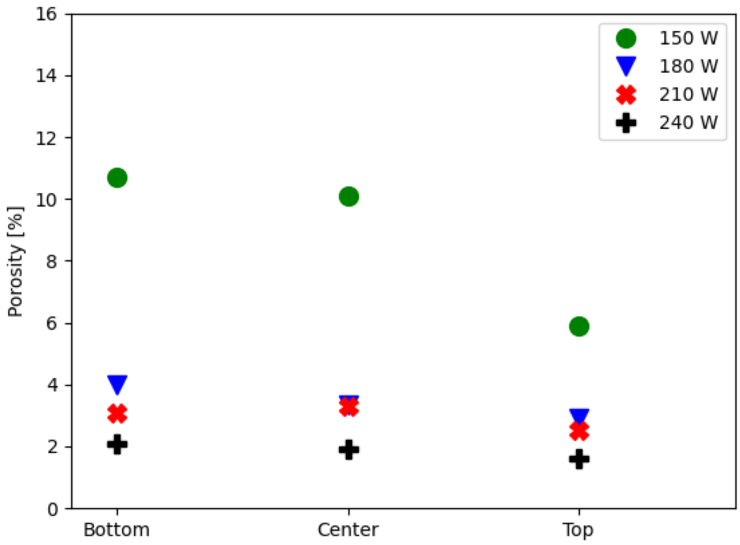

Figure 62 - Porosity variation through the specimen for E_d = 35 J/mm^3

4.3.3 Microstructure

Figure 63 shows microscope images of the cross-section of the samples. Due to the LOF defects present in the samples, in some cases, especially at low energy density, it is not possible to observe the melting pool (i.e., the track of the molten material). Indeed, as suggested by the presence of LOF defects, melting of the powders and thus the formation of melting pool is not achieved. For higher laser power values, it is possible to notice irregular-shaped melting pools, in Figure 64, the micrographs of the samples produced in the limit conditions are shown. In the worst case (= 150 W and = 20 J/ mm^3) the Cu powders remain un-melted and embedded into the Al matrix (Figure 64 panel a), while in the best case (= 240 W and = 35 J/ mm^3) it is possible to appreciate exceptionally fine grains with grain boundaries rich in precipitates (Figure 64 panel b).

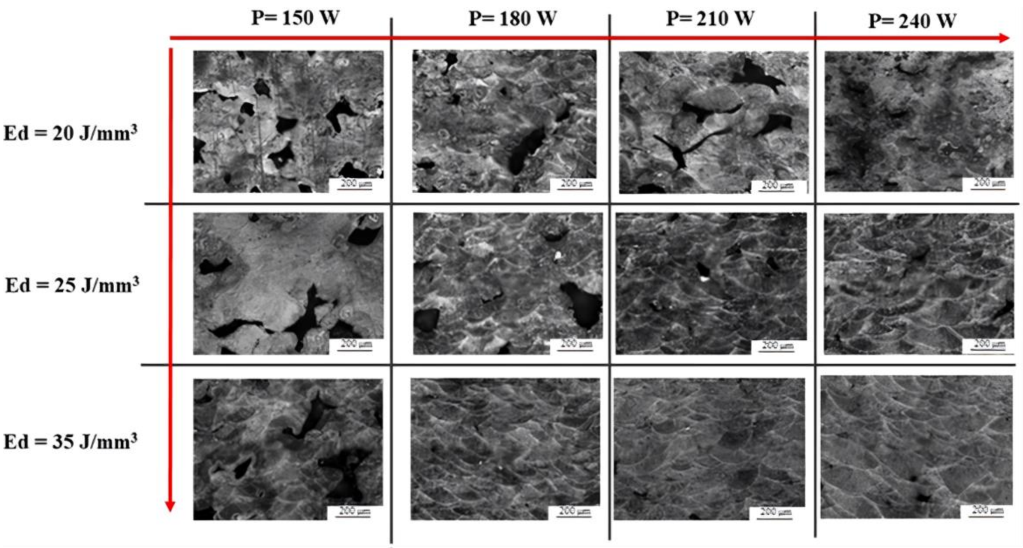

Figure 63 - Microscope images of the cross-section of the samples.

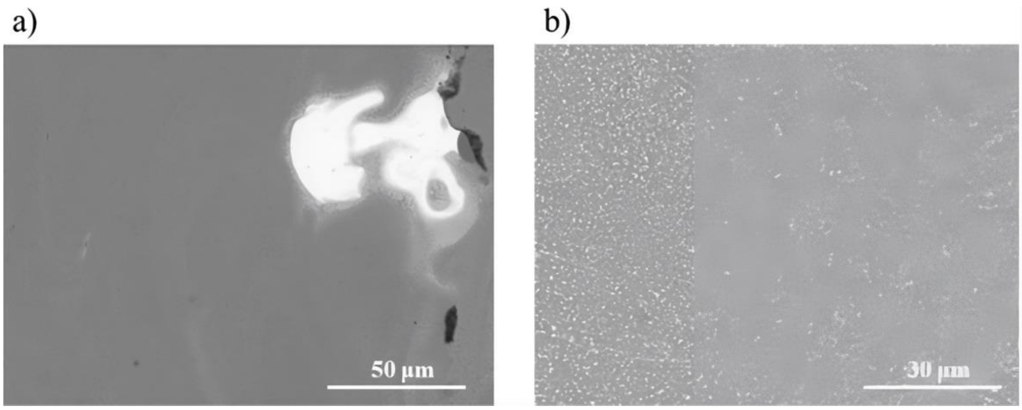

Figure 64 - Micrography of the samples with (a) P = 150 W and Ed = 20 J/mm^3 and (b) P = 240 W and Ed = 35 J/mm^3.

4.3.4 Microhardness

Microhardness can be considered the first indicator for the mechanical quality of the printed material. The results are shown in FIGURE at different laser power and energy density. The values range from 126 HV to 148 HV. While no significant trend can be observed the average microhardness of the samples is 135 HV, similar to what is found in the literature (range 100–150 HV) [68].

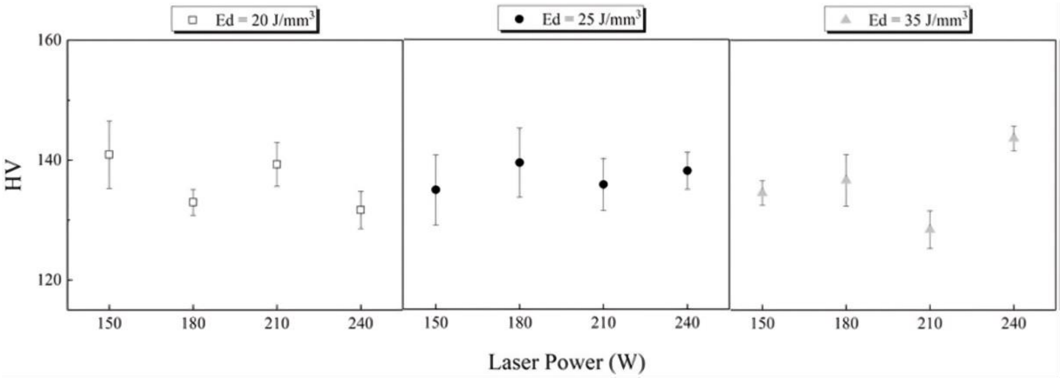

Figure 65 - Microhardness of the samples compared to the laser power and of the energy density.

4.4 Discussion

4.4.1 The role of the powder bed and laser power

All of the results presented above, with the highlighted trends will be discussed taking into specific consideration the impact of the spreading process as it was the main motivation behind this case study. However, other factors influencing the outcome of the process will not be disregarded and will be discussed in due detail. First, it is worth repeating that the features of the substrate can greatly influence the laser-matter interaction. Indeed, Wang et al. [69] demonstrated that the amount of energy adsorbed by a powder bed is different from the one absorbed by the bulk material, due to the different reflection/absorption properties. On this topic, Gusarov et al. [32] studied the transfer of radiation and heat during selective laser melting. They considered a powder bed with porosity corresponding to freely poured powder, which has roughly the values (40–60%) typical for metallic powders employed in SLM. The authors demonstrated that the laser radiation penetrates the substrate via the pores up to several particle diameters of depth due to multiple reflections, confirming that the laser energy is deposited not only on the surface but also in the bulk of the powder layer. This suggests that, along with the laser source wavelength and the corresponding material absorption coefficient, the effective energy transfer from the beam to the powder bed is affected by the powder characteristics (e.g., mixture ratio, particle shape, and size distribution) and the powder bed state. This aspect is even more important for aluminium alloys, which are characterized by high reflectivity. Therefore, a proper choice of the spreading parameters can be pivotal to achieve good densification and suitable mechanical properties of the product. In particular, a higher packing promotes the multiple reflection mechanism and hence the formation of a more stable melting pool at lower laser energy input. By tuning the layer thickness and the spreading speed on the basis of numerical simulations of the spreading process, we have successfully printed an Al-Si-Cu-Mg alloy with a power input significantly lower than the one commonly reported in the literature [6], [7], [59]. The central role and influence of the spreading process can be further inferred from the variation of the LOF defects. Looking at the graphs in Figure 54, a reduction of the number and extension of the LOF defects moving from the bottom to the top zone of the samples is visible, along with better-molten pools. This reduction is more evident for lower values of the laser power. As previously mentioned, such increased quality can be attributed to differences in the spread layer of powders. Indeed, as discussed previously, the characteristics of the deposited layer can change significantly throughout the printing process and therefore, the optimal laser parameters that should be employed from change with the number of printed layers. This aspect is not taken into consideration here, however the results point to the necessity of more in process optimizations. Moreover, looking at the results an influence of the laser power can be observed. Indeed, as also seen by Tang et al. [70], the absorptivity of powders decreases at lower laser power. In agreement with the literature, we have found that the decrease of the laser power leads to an increased formation of LOF defects, even with the same energy density, leading to incomplete remelting of the latest solidified layer and a poor metallurgical bond [71].

4.4.2 Comparison with the literature

In order to showcase the effectiveness of the spreading process optimization in terms of energy efficiency a brief recap of literature works dealing with Al-

Cu-Mg and AlSi10Mg alloys is presented in Table 9. The properties considered are the densification, since it is a key indicator of the quality of the process, and microhardness, since it can be considered as a good indicator of the mechanical properties of the printed part. Moreover, other fundamental mechanical properties (e.g., yield stress) can be derived from microhardness through empirical relationships [72], motivating the adoption of this parameter. An energy efficiency index is also reported, defined as the ratio between *Ed* and HV. While not having a physical meaning, this index allows to immediately compare the results of different processes. As clearly visible in Table 9, the value of the energy density adopted in this work is unprecedently low for this type of alloys, with a significant reduction even when compared with pure AlSi10Mg that is easier to print and more widely studied. Despite the low *Ed* values, the samples produced in the present work show good mechanical properties, leading to a value of (3.8) 80% higher than the best value found in the literature. In Chen et al. [73], where a comparably low *Ed* was selected as the optimal parameter based on a FEM model of the substrate-beam interaction, the resulting mechanical properties are fairly low, suggesting that the selection of printing parameters from an incomplete, although rigorous modelling that does not take into account all the steps of the process can negatively affect the experimental outcomes. It is worth noticing that the value of this parameter spans a wide range of values (0.2–2.1), confirming that the selection of the optimal process parameters is challenging and strictly dependent on the application.

Table 9 - Comparison of SLMed Al-Cu-Mg alloys process parameters and properties as found in the literature.

Material	P [W]	h_s [mm]	L_t [mm]	V_s [mm/s]	Ed [J/mm^3]	Density [%]	HV	η_e	Ref.
AlSi10Mg+Cu	240	0.09	0.05	2133	35	> 97	135	3.86	-
Al+Cu+Mg	200	0.7-0.13	0.04	83-333.3	100-300	94-99	-	-	[59]
Al+Cu+Mg	200	0.7-0.13	0.04	-	>340	99	111	0.32	[59]
Al+Cu+Mg	200	0.09	0.04	83	666	99.91	125	0.19	[6]
Al+Cu	190	0.08	0.04	165	359.8	99 ±1	-	-	[60]
AlSi10Mg	280	0.03	0.06	2000	77.78	-	125	1.61	[61]
AlSi10Mg	330	0.16	0.03	1000	50-60	99.70	-	-	[62]
AlSi10Mg	250	0.07	0.03	2100	56.7	99	116	2.04	[63]
AlSi10Mg	280	0.05-0.07	0.03	800-1300	116-183	> 97	-	-	[64]
AlSi10Mg	330	0.19	0.03	1300	44.53	-	95	2.13	[73]

Section 5: Future developments

Physics based Discrete Element Method simulations are accurate and reproducible, however are really demanding in terms of computational power required. It has been pointed out numerous times throughout the previous two chapters that it was needed to introduce simplifying assumptions to avoid excessive computational time. Therefore, some kind of reduced model would be pivotal to fully unlock the spreading process optimization. Indeed, a model with some degree of real time predictive capabilities on the characteristics of the powder bed in function of the process variables would be fundamental for actual applications in an industrial environment. In general, there exists a literature dealing with the application of Machine Learning to metal Additive Manufacturing, ranging from the design to the parameter optimization and quality control [74]. Considering the powder spreading stage most of the works make use of computer vision techniques and Convolutional Neural Networks to monitor the state of the powder bed and classify defects [75] in order to propose correctional procedures. The work from Desai et al. [31] uses a DEM based model to generate the data to train a feed forward neural network. A similar approach was followed in this thesis, where the presented model was used to generate a training dataset.

Among the multitude of machine learning architectures, the choice fell on Gaussian process regression. The Gaussian processes model is a probabilistic supervised machine learning framework that has been widely used for regression and classification tasks. A Gaussian processes regression (GPR) model can make predictions incorporating prior knowledge (kernels) and provide uncertainty measures over predictions [76]. A complete description of the mathematical basis and the functioning principle of the method will not be discussed here but can be found in the reference.

The main reasons a GPR was selected is due to the nature of the dataset. Indeed, Gaussian processes do not need an extensive number of train data point to output a prediction. Another great feature of Gaussian processes is that the uncertainty of a fitted GP increases away from the training data, but this uncertainty is known and can be paired with an optimization algorithm to identify the best point to reduce said uncertainty. This proposition of sampling points in is done by acquisition functions which usually trade off exploitation and exploration. Exploration refers to sampling in areas where the prediction uncertainty is large while exploitation refers to sampling where the output is significant. All of these characteristics fit the needs in this case.

The input and output for our model will be the same presented in section 3.4. First, a GP is built based on the assumption that the input parameters completely describe the state of the powder bed. Therefore, every layer of every simulation becomes a new point with its input and output. However, the results of this more general model are not satisfactory and completely fail to capture the variation of the outputs with the layer.

Therefore, we are now considering two separate models: a layer-wise model

$$M_1(roughness, VL) \rightarrow (outputs)$$

Which aims to predict the variation of the outputs with different layers, for fixed user defined inputs.

And a variable-wise model which aims to predict the characteristics of the powder bed at the steady state.

$$M_2(Roughness, ELT, Recoating\ speed) \rightarrow (outputs@stable\ )$$

These two separate models granted more promising results; however, much remains to be to obtain a reliable prediction from the models specifically from the gaussian process modelling point of view (e.g., kernel, acquisition function etc.)

Section 6: Conclusions

In this thesis, the spreading stage of a LPBF process has been investigated with a combined experimental and numerical approach. In the first section the development of a custom-made recoating device was presented along with the results of the experiments carried out on it. The main findings can be summarized as follows:

- A variation in the spreading speed is beneficial or detrimental based on the ratio between the feedstock particles diameter and the nominal layer thickness.
- A higher spreading speed promotes segregation of the bigger particles towards the end of the deposition plate while a slower spreading speed promotes the opposite phenomenon.
- Overall, the effect of the spreading parameters is strongly dependent on the characteristics of the feedstock material and any optimization should be performed taking it into account.

The second section presents the implementation of a Discrete Element Method based model which is used to investigate the spreading process and identify the mechanisms taking place at a particle level. First, a simple single layer model is used to understand the impact of the process parameters (i.e., layer thickness and spreading speed).

- For a higher spreading speed, a lower amount of the total powder in the powder reservoir after the spreading process can be observed, further suggesting the necessity to vary the total quantity of powder to be spread.

- The initial and the terminal zones of the bed are affected in different ways by the interaction with a solid part (the powder bed chamber in this case), thus leading to an alteration of the bed characteristics.
- The described spreading mechanisms are prone to cause further particles segregation during the deposition stage. This appears to be more evident when the speed of the blade is low since, for higher velocities, these segregation phenomena are overwhelmed by the dynamic effects.

The model is then extended to take into account the multi-layer nature of the process. The behaviour observed for a single layer could still be appreciated to some degree, however, a significant variation in the powder bed characteristics emerges throughout the layers. It appears that a stable state is reached after a certain number of layers which depends strongly on the process parameters. Specifically, a lower spreading speed promotes the attainment of this stable state in fewer layers. A strategy to freeze part of the powder bed is also proposed with the aim of understanding the impact of the previous layer characteristics on the spreading process. Overall, the proposed numerical model highlights specific mechanisms involved during the blade motion that may be detrimental for the final state of the powder bed. We believe that the present analysis can help to properly set the parameters of the spreading process and design novel printing machines to improve the quality of the spread powder and of the resulting final material.

To show the applicability of the presented model a case study is also considered. This case study showed how the energy efficiency of a 3D printing of a custom Al-Cu alloy can be improved via an optimized spreading stage, aimed at improving the absorptivity of the powder bed. Despite the limitations of the numerical model used, the positive correlation is evident, suggesting that a far more advanced optimization strategy could further improve the results leading to more efficient processes overall. Preliminary results on the application of machine learning techniques to the spreading process are also presented but, despite the promising premises, further investigations are needed to attain satisfactory results.

Bibliography

[1] K. v. Wong and A. Hernandez, “A Review of Additive Manufacturing,” *ISRN Mechanical Engineering*, vol. 2012, pp. 1–10, 2012, doi: 10.5402/2012/208760.

[2] H. Gong, K. Rafi, H. Gu, T. Starr, and B. Stucker, “Analysis of defect generation in Ti-6Al-4V parts made using powder bed fusion additive manufacturing processes,” *Addit Manuf*, vol. 1, pp. 87–98, 2014, doi: 10.1016/j.addma.2014.08.002.

[3] W. E. Frazier, “Metal additive manufacturing: A review,” *Journal of Materials Engineering and Performance*, vol. 23, no. 6. pp. 1917–1928, 2014. doi: 10.1007/s11665-014-0958-z.

[4] L. zhi Wang, S. Wang, and X. Hong, “Pulsed SLM-manufactured AlSi10Mg alloy: Mechanical properties and microstructural effects of designed laser energy densities,” *Journal of Manufacturing Processes*, vol. 35. pp. 492–499, 2018. doi: 10.1016/j.jmapro.2018.09.007.

[5] H. Shipley *et al.*, “Optimisation of process parameters to address fundamental challenges during selective laser melting of Ti-6Al-4V: A review,” *Int J Mach Tools Manuf*, vol. 128, no. September 2017, pp. 1–20, 2018, doi: 10.1016/j.ijmachtools.2018.01.003.

[6] X. Nie, H. Zhang, H. Zhu, Z. Hu, L. Ke, and X. Zeng, “Analysis of processing parameters and characteristics of selective laser melted high strength Al-Cu-Mg alloys: From single tracks to cubic samples,” *J Mater Process Technol*, vol. 256, no. January, pp. 69–77, 2018, doi: 10.1016/j.jmatprotec.2018.01.030.

[7] R. della Gatta, I. del Sol, A. Caraviello, and A. Astarita, “Selective laser melting of an Al-Si-Mg-Cu alloy: feasibility and processing aspects,” *Materials and Manufacturing Processes*, vol. 36, no. 12, pp. 1438–1449, Sep. 2021, doi: 10.1080/10426914.2021.1906900.

[8] O. B. Kovalev, A. v. Gusarov, and V. v. Belyaev, “Morphology of random packing of micro-particles and its effect on the absorption of laser radiation during selective melting of powders,” *Int J Eng Sci*, vol. 157, p. 103378, 2020, doi: 10.1016/j.ijengsci.2020.103378.

[9] J. Zhang *et al.*, “Influence of Particle Size on Laser Absorption and Scanning Track Formation Mechanisms of Pure Tungsten Powder During Selective Laser Melting,” *Engineering*, vol. 5, no. 4, pp. 736–745, 2019, doi: 10.1016/j.eng.2019.07.003.

[10] V. Lampitella, M. Trofa, A. Astarita, and G. D’Avino, “Discrete Element Method Analysis of the Spreading Mechanism and Its Influence on Powder Bed Characteristics in Additive Manufacturing,” *Micromachines (Basel)*, vol. 12, no. 4, p. 392, 2021, doi: 10.3390/mi12040392.

[11] A. Mostafaei *et al.*, “Defects and anomalies in powder bed fusion metal additive manufacturing,” *Curr Opin Solid State Mater Sci*, vol. 26, no. 2, p. 100974, Apr. 2022, doi: 10.1016/j.cossms.2021.100974.

[12] M. Kalms, R. Narita, C. Thomy, F. Vollertsen, and R. B. Bergmann, “New approach to evaluate 3D laser printed parts in powder bed fusion-based additive manufacturing in-line within closed space,” *Addit Manuf*, vol. 26, pp. 161–165, 2019, doi: 10.1016/j.addma.2019.01.011.

[13] P. J. DePond *et al.*, “In situ measurements of layer roughness during laser powder bed fusion additive manufacturing using low coherence scanning interferometry,” *Mater Des*, vol. 154, pp. 347–359, 2018, doi: 10.1016/j.matdes.2018.05.050.

[14] Y. Liu, L. Blunt, Z. Zhang, H. A. Rahman, F. Gao, and X. Jiang, “In-situ areal inspection of powder bed for electron beam fusion system based on fringe projection profilometry,” *Addit Manuf*, vol. 31, p. 100940, Jan. 2020, doi: 10.1016/j.addma.2019.100940.

[15] U. Ali *et al.*, “On the measurement of relative powder-bed compaction density in powder-bed additive manufacturing processes,” *Mater Des*, vol. 155, pp. 495–501, Oct. 2018, doi: 10.1016/j.matdes.2018.06.030.

[16] G. Jacob, A. Donmez, J. Slotwinski, and S. Moylan, “Measurement of powder bed density in powder bed fusion additive manufacturing processes,” *Meas Sci Technol*, vol. 27, no. 11, p. 115601, Nov. 2016, doi: 10.1088/0957-0233/27/11/115601.

[17] M. Ahmed, M. Pasha, W. Nan, and M. Ghadiri, “A simple method for assessing powder spreadability for additive manufacturing,” *Powder*

Technology, vol. 367. Elsevier B.V., pp. 671–679, May 01, 2020. doi: 10.1016/j.powtec.2020.04.033.

[18] P. A. Cundall and O. D. L. Strack, "A discrete numerical model for granular assemblies," *Géotechnique*, vol. 29, no. 1, pp. 47–65, Mar. 1979, doi: 10.1680/geot.1979.29.1.47.

[19] M. Trofa, G. D'Avino, B. Fabiano, and M. Vocciante, "Nanoparticles synthesis in wet-operating stirred media: Investigation on the grinding efficiency," *Materials*, vol. 13, no. 19, 2020, doi: 10.3390/MA13194281.

[20] J. Lohaus, Y. M. Perez, and M. Wessling, "What are the microscopic events of colloidal membrane fouling?," *J Memb Sci*, vol. 553, pp. 90–98, May 2018, doi: 10.1016/j.memsci.2018.02.023.

[21] E. J. R. Parteli and T. Pöschel, "Particle-based simulation of powder application in additive manufacturing," *Powder Technol*, vol. 288, pp. 96–102, 2016, doi: 10.1016/j.powtec.2015.10.035.

[22] H. W. Mindt, M. Megahed, N. P. Lavery, M. A. Holmes, and S. G. R. Brown, "Powder Bed Layer Characteristics: The Overseen First-Order Process Input," *Metall Mater Trans A Phys Metall Mater Sci*, 2016, doi: 10.1007/s11661-016-3470-2.

[23] S. Haeri, Y. Wang, O. Ghita, and J. Sun, "Discrete element simulation and experimental study of powder spreading process in additive manufacturing," *Powder Technol*, vol. 306, pp. 45–54, 2017, doi: 10.1016/j.powtec.2016.11.002.

[24] H. Chen, Q. Wei, Y. Zhang, F. Chen, Y. Shi, and W. Yan, "Powder-spreading mechanisms in powder-bed-based additive manufacturing: Experiments and computational modeling," *Acta Mater*, vol. 179, pp. 158–171, 2019, doi: 10.1016/j.actamat.2019.08.030.

[25] C. Meier, R. Weissbach, J. Weinberg, W. A. Wall, and A. J. Hart, "Critical influences of particle size and adhesion on the powder layer uniformity in metal additive manufacturing," *J Mater Process Technol*, vol. 266, pp. 484–501, Apr. 2019, doi: 10.1016/j.jmatprotec.2018.10.037.

[26] S. Haeri, “Optimisation of blade type spreaders for powder bed preparation in Additive Manufacturing using DEM simulations,” *Powder Technol*, 2017, doi: 10.1016/j.powtec.2017.08.011.

[27] W. Nan *et al.*, “Jamming during particle spreading in additive manufacturing,” *Powder Technol*, vol. 338, pp. 253–262, Oct. 2018, doi: 10.1016/j.powtec.2018.07.030.

[28] J. Zhang, Y. Tan, T. Bao, Y. Xu, X. Xiao, and S. Jiang, “Discrete Element Simulation of the Effect of Roller-Spreading Parameters on Powder-Bed Density in Additive Manufacturing,” *Materials*, vol. 13, no. 10, p. 2285, May 2020, doi: 10.3390/ma13102285.

[29] Y. M. Fouda and A. E. Bayly, “A DEM study of powder spreading in additive layer manufacturing,” *Granul Matter*, vol. 22, no. 1, 2020, doi: 10.1007/s10035-019-0971-x.

[30] Q. Han, H. Gu, and R. Setchi, “Discrete element simulation of powder layer thickness in laser additive manufacturing,” *Powder Technol*, 2019, doi: 10.1016/j.powtec.2019.04.057.

[31] P. S. Desai and C. Fred Higgs, “Spreading process maps for powder-bed additive manufacturing derived from physics model-based machine learning,” *Metals (Basel)*, 2019, doi: 10.3390/met9111176.

[32] A. v. Gusarov, I. Yadroitsev, P. Bertrand, and I. Smurov, “Model of radiation and heat transfer in laser-powder interaction zone at selective laser melting,” *J Heat Transfer*, vol. 131, no. 7, pp. 1–10, 2009, doi: 10.1115/1.3109245.

[33] M. Fousová, D. Vojtěch, K. Doubrava, M. Daniel, and C. F. Lin, “Influence of inherent surface and internal defects on mechanical properties of additively manufactured Ti6Al4V alloy: Comparison between selective laser melting and electron beam melting,” *Materials*, vol. 11, no. 4, 2018, doi: 10.3390/ma11040537.

[34] A. K. Singla *et al.*, “Selective laser melting of Ti6Al4V alloy: Process parameters, defects and post-treatments,” *J Manuf Process*, vol. 64, no. January, pp. 161–187, 2021, doi: 10.1016/j.jmapro.2021.01.009.

[35] N. Béraud, F. Vignat, F. Villeneuve, and R. Dendievel, “Improving dimensional accuracy in EBM using beam characterization and

trajectory optimization," *Addit Manuf*, vol. 14, pp. 1–6, Mar. 2017, doi: 10.1016/j.addma.2016.12.002.

[36] Y. Mahmoodkhani *et al.*, "On the measurement of effective powder layer thickness in laser powder-bed fusion additive manufacturing of metals," *Progress in Additive Manufacturing*, vol. 4, no. 2, pp. 109–116, Jun. 2019, doi: 10.1007/s40964-018-0064-0.

[37] M. Y. Shaheen, A. R. Thornton, S. Luding, and T. Weinhart, "The influence of material and process parameters on powder spreading in additive manufacturing," *Powder Technol*, vol. 383, pp. 564–583, 2021, doi: 10.1016/j.powtec.2021.01.058.

[38] D. Yao *et al.*, "Dynamic investigation on the powder spreading during selective laser melting additive manufacturing," *Addit Manuf*, vol. 37, no. November 2020, p. 101707, 2021, doi: 10.1016/j.addma.2020.101707.

[39] L. I. Escano *et al.*, "Revealing particle-scale powder spreading dynamics in powder-bed-based additive manufacturing process by high-speed x-ray imaging," *Sci Rep*, vol. 8, no. 1, pp. 1–11, 2018, doi: 10.1038/s41598-018-33376-0.

[40] R. D. Mindlin and H. Deresiewicz, "Elastic Spheres in Contact Under Varying Oblique Forces," in *The Collected Papers of Raymond D. Mindlin Volume I*, 1989. doi: 10.1007/978-1-4613-8865-4_35.

[41] T. Roessler and A. Katterfeld, "Scaling of the angle of repose test and its influence on the calibration of DEM parameters using upscaled particles," *Powder Technol*, 2018, doi: 10.1016/j.powtec.2018.01.044.

[42] Z. Yan, S. K. Wilkinson, E. H. Stitt, and M. Marigo, "Discrete element modelling (DEM) input parameters: understanding their impact on model predictions using statistical analysis," *Comput Part Mech*, 2015, doi: 10.1007/s40571-015-0056-5.

[43] E. Hosseini and V. A. Popovich, "A review of mechanical properties of additively manufactured Inconel 718," *Additive Manufacturing*. 2019. doi: 10.1016/j.addma.2019.100877.

[44] A. T. Sutton, C. S. Kriewall, M. C. Leu, and J. W. Newkirk, "Powder characterisation techniques and effects of powder characteristics on

part properties in powder-bed fusion processes," *Virtual and Physical Prototyping*. 2017. doi: 10.1080/17452759.2016.1250605.

[45] Y. C. Zhou, B. D. Wright, R. Y. Yang, B. H. Xu, and A. B. Yu, "Rolling friction in the dynamic simulation of sandpile formation," *Physica A: Statistical Mechanics and its Applications*, 1999, doi: 10.1016/S0378-4371(99)00183-1.

[46] M. Alizadeh, M. Asachi, M. Ghadiri, A. Bayly, and A. Hassanpour, "A methodology for calibration of DEM input parameters in simulation of segregation of powder mixtures, a special focus on adhesion," *Powder Technol*, 2018, doi: 10.1016/j.powtec.2018.08.028.

[47] P. S. Desai, A. Mehta, P. S. M. Dougherty, and F. C. Higgs, "A rheometry based calibration of a first-order DEM model to generate virtual avatars of metal Additive Manufacturing (AM) powders," *Powder Technol*, 2019, doi: 10.1016/j.powtec.2018.09.047.

[48] S. Kirsch, "Avoiding ambiguity in DEM in-situ calibration for dry bulk materials," *Miner Eng*, 2020, doi: 10.1016/j.mineng.2019.106094.

[49] T. Roessler, C. Richter, A. Katterfeld, and F. Will, "Development of a standard calibration procedure for the DEM parameters of cohesionless bulk materials – part I: Solving the problem of ambiguous parameter combinations," *Powder Technol*, 2019, doi: 10.1016/j.powtec.2018.11.034.

[50] S. Geer, M. L. Bernhardt-Barry, E. J. Garboczi, J. Whiting, and A. Donmez, "A more efficient method for calibrating discrete element method parameters for simulations of metallic powder used in additive manufacturing," *Granul Matter*, 2018, doi: 10.1007/s10035-018-0848-4.

[51] J. B. Knight, E. E. Ehrichs, V. Y. Kuperman, J. K. Flint, H. M. Jaeger, and S. R. Nagel E, "Experimental study of granular convection," *Phys Rev E Stat Phys Plasmas Fluids Relat Interdiscip Topics*, 1996, doi: 10.1103/physreve.54.5726.

[52] C. Kloss, C. Goniva, A. Hager, S. Amberger, and S. Pirker, "Models, algorithms and validation for opensource DEM and CFD-DEM,"

Progress in Computational Fluid Dynamics, 2012, doi: 10.1504/PCFD.2012.047457.

[53] S. Plimpton, "Fast Parallel Algorithms for Short-Range Molecular Dynamics," *J Comput Phys*, vol. 117, no. 1, pp. 1–19, Mar. 1995, doi: 10.1006/JCPH.1995.1039.

[54] R. Berger, C. Kloss, A. Kohlmeyer, and S. Pirker, "Hybrid parallelization of the LIGGGHTS open-source DEM code," *Powder Technol*, vol. 278, pp. 234–247, Jul. 2015, doi: 10.1016/j.powtec.2015.03.019.

[55] T. M. Wischeropp, C. Emmelmann, M. Brandt, and A. Pateras, "Measurement of actual powder layer height and packing density in a single layer in selective laser melting," *Additive Manufacturing*, vol. 28. Elsevier B.V., pp. 176–183, Aug. 01, 2019. doi: 10.1016/j.addma.2019.04.019.

[56] D. Jansen, T. Hanemann, M. Radek, A. Rota, J. Schröpfer, and M. Heilmaier, "Development of actual powder layer height depending on nominal layer thicknesses and selection of laser parameters," *J Mater Process Technol*, vol. 298, Dec. 2021, doi: 10.1016/j.jmatprotec.2021.117305.

[57] T. T. Roehling *et al.*, "Modulating laser intensity profile ellipticity for microstructural control during metal additive manufacturing," *Acta Mater*, vol. 128, pp. 197–206, Apr. 2017, doi: 10.1016/j.actamat.2017.02.025.

[58] J. H. Martin, B. D. Yahata, J. M. Hundley, J. A. Mayer, T. A. Schaedler, and T. M. Pollock, "3D printing of high-strength aluminium alloys," *Nature*, vol. 549, no. 7672, pp. 365–369, 2017, doi: 10.1038/nature23894.

[59] H. Zhang, H. Zhu, T. Qi, Z. Hu, and X. Zeng, "Selective laser melting of high strength Al-Cu-Mg alloys: Processing, microstructure and mechanical properties," *Materials Science and Engineering A*, vol. 656, pp. 47–54, 2016, doi: 10.1016/j.msea.2015.12.101.

[60] P. Wang, L. Deng, K. G. Prashanth, S. Pauly, J. Eckert, and S. Scudino, "Microstructure and mechanical properties of Al-Cu alloys fabricated by selective laser melting of powder mixtures," *J Alloys*

Compd, vol. 735, pp. 2263–2266, 2018, doi: 10.1016/j.jallcom.2017.10.168.

[61] M. Ghasri-Khouzani *et al.*, "Comparing microstructure and hardness of direct metal laser sintered AlSi10Mg alloy between different planes," *J Manuf Process*, vol. 37, no. March 2018, pp. 274–280, 2019, doi: 10.1016/j.jmapro.2018.12.005.

[62] A. H. Maamoun, Y. F. Xue, M. A. Elbestawi, and S. C. Veldhuis, "Effect of selective laser melting process parameters on the quality of al alloy parts: Powder characterization, density, surface roughness, and dimensional accuracy," *Materials*, vol. 11, no. 12, 2018, doi: 10.3390/ma11122343.

[63] X. Teng *et al.*, "Parameter optimization and microhardness experiment of AlSi10Mg alloy prepared by selective laser melting," *Mater Res Express*, vol. 6, no. 8, 2019, doi: 10.1088/2053-1591/ab18d0.

[64] Z. Chen *et al.*, "Experimental Research on Selective Laser Melting AlSi10Mg Alloys: Process, Densification and Performance," *J Mater Eng Perform*, vol. 26, no. 12, pp. 5897–5905, 2017, doi: 10.1007/s11665-017-3044-5.

[65] A. Hatem, C. Schulz, T. Schlaefer, J. T. Boobhun, N. Stanford, and C. Hall, "Influence of laser absorption by water- and gas-atomised powder feedstock on Laser Metal Deposition of AISI 431 stainless steel," *Addit Manuf*, vol. 47, no. August, p. 102242, 2021, doi: 10.1016/j.addma.2021.102242.

[66] International Organization for Standardization, *ISO 25178-2: Geometrical product specifications (GPS) - Surface texture: Areal Part - 2: Terms, definitions and surface texture parameters*. 2007.

[67] T. Montalbano *et al.*, "Uncovering the coupled impact of defect morphology and microstructure on the tensile behavior of Ti-6Al-4V fabricated via laser powder bed fusion," *J Mater Process Technol*, 2021, doi: 10.1016/j.jmatprotec.2021.117113.

[68] D. Buchbinder, H. Schleifenbaum, S. Heidrich, W. Meiners, and J. Bültmann, "High power Selective Laser Melting (HP SLM) of aluminum parts," in *Physics Procedia*, 2011. doi: 10.1016/j.phpro.2011.03.035.

[69] X. C. Wang, T. Laoui, J. Bonse, J. P. Kruth, B. Lauwers, and L. Froyen, “Direct selective laser sintering of hard metal powders: Experimental study and simulation,” *International Journal of Advanced Manufacturing Technology*, vol. 19, no. 5, pp. 351–357, 2002, doi: 10.1007/s001700200024.

[70] M. Tang, P. C. Pistorius, and J. L. Beuth, “Prediction of lack-of-fusion porosity for powder bed fusion,” *Addit Manuf*, vol. 14, pp. 39–48, 2017, doi: 10.1016/j.addma.2016.12.001.

[71] R. Xiao and X. Zhang, “Problems and issues in laser beam welding of aluminum-lithium alloys,” *Journal of Manufacturing Processes*. 2014. doi: 10.1016/j.jmapro.2013.10.005.

[72] M. Tiryakioğlu, “On the relationship between Vickers hardness and yield stress in Al-Zn-Mg-Cu Alloys,” *Materials Science and Engineering A*, vol. 633, pp. 17–19, 2015, doi: 10.1016/j.msea.2015.02.073.

[73] J. CHEN, W. HOU, X. WANG, S. CHU, and Z. YANG, “Microstructure, porosity and mechanical properties of selective laser melted AlSi10Mg,” *Chinese Journal of Aeronautics*, vol. 33, no. 7, pp. 2043–2054, 2020, doi: 10.1016/j.cja.2019.08.017.

[74] C. Wang, X. P. Tan, S. B. Tor, and C. S. Lim, “Machine learning in additive manufacturing: State-of-the-art and perspectives,” *Additive Manufacturing*, vol. 36. Elsevier B.V., Dec. 01, 2020. doi: 10.1016/j.addma.2020.101538.

[75] L. Scime and J. Beuth, “A multi-scale convolutional neural network for autonomous anomaly detection and classification in a laser powder bed fusion additive manufacturing process,” *Addit Manuf*, vol. 24, pp. 273–286, Dec. 2018, doi: 10.1016/j.addma.2018.09.034.

[76] C. Edward. Rasmussen and C. K. I. Williams, *Gaussian processes for machine learning*. MIT Press, 2006.